SANDIA REPORT

SAND2002-3615
Unlimited Release
Printed November 2002

All-Ceramic Thin Film Battery

T. J. Boyle, D. Ingersoll, R. T. Cygan, M. A. Rodriguez, K. Rahimian, J.A. Voight

Prepared by
Sandia National Laboratories
Albuquerque, New Mexico 87185 and Livermore, California 94550

Sandia is a multiprogram laboratory operated by Sandia Corporation, a Lockheed Martin Company, for the United States Department of Energy under Contract DE-AC04-94AL85000.

Issued by Sandia National Laboratories, operated for the United States Department of Energy by Sandia Corporation.

SAND2002-3615
Unlimited Release
Printed November 2002

All-Ceramic Thin Film Battery

Timothy J. Boyle
Chemical Sythesis and Nanomaterials

David Ingersoll,
Lithium Battery Research and Development

Randall T. Cygan,
Geochemistry

Mark A. Rodriguez,
Materials Characterization

Kamyar Rahimian,
Chemical Sythesis and Nanomaterials

James A. Voigt
Chemical Sythesis and Nanomaterials

Sanida National Laboratories
P.O. Box 5800
Albuquerque, NM 87185-1349

1. Abstract

We have undertaken the synthesis of a thin film "All Ceramic Battery" (ACB) using solution route processes. Based on the literature and experimental results, we selected SnO_2, $LiCoO_2$, and

$LiLaTiO_3$ (LLT) as the anode, cathode, and electrolyte, respectively. Strain induced by lattice mismatch between the cathode and bottom electrode, as estimated by computational calculations, indicate that thin film orientations for batteries when thicknesses are as low as 500 Å are strongly controlled by surface energies. Therefore, we chose platinized silicon as the basal platform based on our previous experience with this material. The anode thin films were generated by standard spin-cast methods and processing using a solution of $[Sn(ONep)]_8$ and HOAc which was found to form $Sn_6(O)_4(ONep)_4$. Electrochemical evaluation showed that the SnO_2 was converted to Sn° during the first cycle. The cathode was also prepared by spin coating using the novel $[Li(ONep)]_8$ and $Co(OAc)_2$. The films could be electrochemically cycled (i.e., charged/discharged), with all of the associated structural changes being observable by XRD. Computational models indicated that the LLT electrolyte would be the best available ceramic material for use as the electrolyte. The LLT was synthesized from $[Li(ONep)]_8$, $[Ti(ONep)_4]_2$, and $La(DIP)_3(py)_3$ with RTP processing at 900 °C being necessary to form the perovskite phase. Alternatively, a novel route to thin films of the block co-polymer ORMOLYTE was developed. The integration of these components was undertaken with each part of the assembly being identifiably by XRD analysis (this will allow us to follow the progress of the charge/discharge cycles of the battery during use!). SEM investigations revealed the films were continuous with minimal mixing. All initial testing of the thin-film cathode/electrolyte/anode ACB devices revealed electrical shorting. Alternative approaches for preparing non-shorted devices (e.g. inverted and side-by-side) are under study.

2. Table of Contents

List of Figures

3. Introduction

The development of small, light-weight, power sources is being driven by the desire/need for smaller electronic devices and emerging technologies, such as the autonomous micro-and meso-machines (MEMS) which are be developed for use as early warning detection agents in the fight against terrorism and/or counter proliferation. Power sources that possess the requisite power and energy to operate these small devices, such as micro-machines, sensors, transmitters, and other electronic circuitry without substantially increasing the final size of the device are necessary to achieve autonomy as well as to aid in the covert nature of some of these devices. Currently, these MEMS devices are being operated by very large power sources, in comparison to the final device size. An integrated power source that will not substantially increase the weight or size of the device that can be conformally added to a device is of high interest. Thin film batteries are an attractive alternative power source for these applications; however, existing thin film batteries are inadequate to meet these needs.[1-5]

The technology developed in this program focused on a rechargeable thin film all-ceramic battery (ACB) fabricated using a fast, inexpensive solution process approach that can be conformally coated onto a variety of surfaces as a thin layer device (thinner than a sheet of paper) that will meet the above needs. Figures 1 and 2 show diagrammatic representations of the proposed design. This ability to design devices with the power source as an integral part of the system will add flexibility to the design of technologies, as well as reducing weight of the device without sacrificing mission capabilities. For example, (i) the conformal coatings will allow for realization of Robug and Robug-like technologies; (ii) the development of the small high power

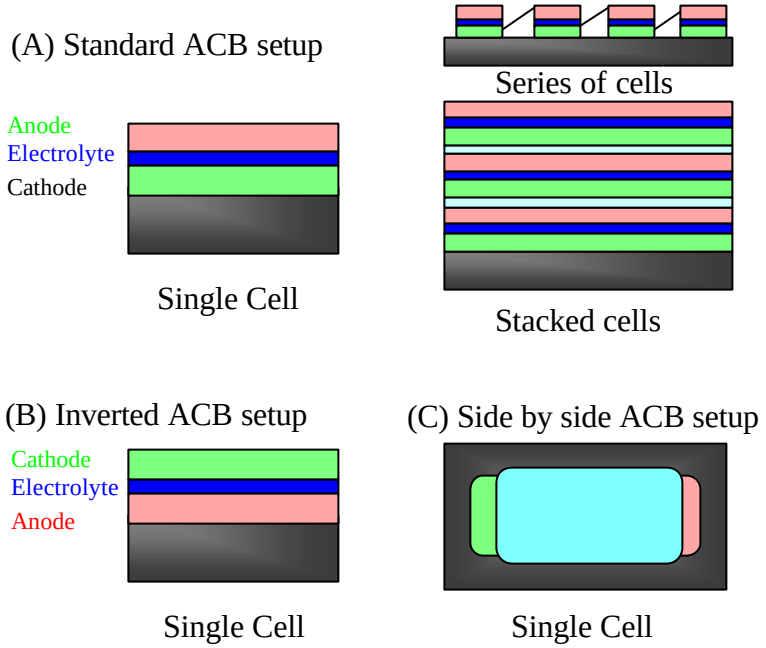

Figure 1. Schematic representation of the ACB setup
(A) standard, (B) Inverted, (C) side-by-side

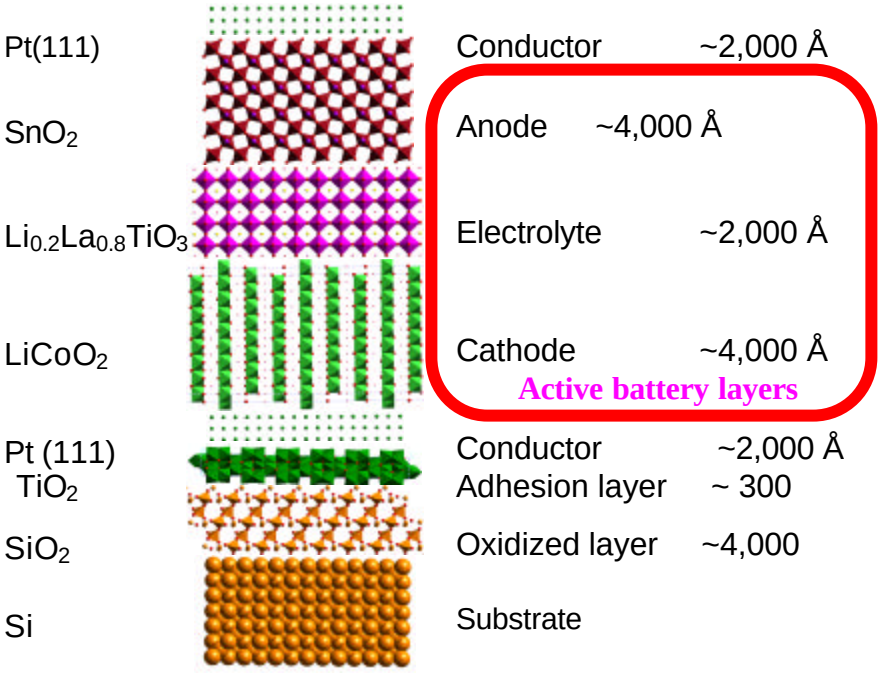

Figure 2. Computational Model of ACB layers

ACB will allow for MEMS devices to truly become autonomous and therefore can be placed directly on small instruments like Robugs; (iii) the development of ACB battery pack will allow for lightweight multi-packs which can be combined to power larger pieces of equipment without substantially increasing the weight a soldier carries (Velcro pack on each vest).

Methods for fabrication of all of the individual elements of the ACB system (anode, cathode, and electrolyte) have been developed. This includes methods for creating thin films of the current collectors for both the positive (cathode) and negative (anode) cell terminals, as well as for both the positive and negative battery active materials. We have also demonstrated fabrication of an entire stack using the functional elements so far developed in combination with a comparable substitute for the electrolyte, and the thin film systems are robust and inconspicuous. The thin film configuration also lends itself to a wide variety of series/parallel interconnect schemes, allowing for wide variability in the performance (e.g., power, run time, etc) of the system. The various aspects of the individual components are discussed below. Further attempts to integrate these components and the computer modeling are also presented.

4. Anode.

We initially focused on eliminating an active lithium layer in the thin film system due to its extreme air sensitivity. Reports from Japan indicate that tin oxide may work as an acceptable anode for lithium ion batteries. Therefore, we undertook the synthesis of a sol-gel precursor solution to generate cassiterite thin films. (Alternatively, lithium metal as the active anode could be generated *in-situ* in the sealed cell during the first electrochemical charge.)

Synthesis/Characterization. Surprisingly only a few simple tin alkoxides ($Sn(OR)_x$) species have been crystallography characterized, including four Sn(IV) complexes $[Sn(OR)_4(HOR)]_2$ (OR = $OCHMe_2$[6,7] or $OCH_2C(H)Me_2$[8]), $Sn(OCMe_3)_4$[6], $[Sn(OCH_2Ph)_4(HN(CH_3)_2)]_2$[9], and two Sn(II) dinuclear complex, $[Sn(OCMe_3)_2]_2$,[10,11] $[Sn(OC(CH_3)_2\text{-}C_6H_4)_2]_2$[9], $Sn(OCH(CF_3)_2)_4 \bullet HNMe_2$[12] and $Sn(OCH(CF_3)_2)_2 \bullet HNMe_2$[13]. A number of Sn(II) and (IV) aryloxide species have been characterized as mono- and di-nuclear due to the steric bulk of the ring substituent.[9] Studies on the hydrolysis of $Sn(OR)_x$ precursors to cassiterite particles have been presented[14-21] wherein some of these investigations have reported a two-step hydrolysis mechanism[20,21] with the majority of hydrolyzed species isolated as $Sn_6(\mu_3\text{-}O)_4(\mu_3\text{-}OR)_4$ (OR = OH[17], OMe[18], $OCHMe_2$[19], $OSiMe_3$[22]). A $Sn_3(O)(OCH_2C(H)Me_2)_{10} \bullet 2(HOCH_2C(H)Me_2)$ complex was also identified.[23]

We undertook the synthesis of Sn(II) alkoxides using tridentate (tris(hydroxymethyl ethane, $(OCH_2)_3C(CH_3)$, THME-H_3), bidentate (carboxylates, O_2CC-R, ORc), and monodentate (*neo*-pentoxide, OC_5H_{11}, ONep) ligands. The THME-ligated species did not form high quality films due to their relative stability in the presence of ambient water. Work with the ORc ligands is currently being investigated with several unique structures being isolated. Therefore, we initiated studies with the mondoentate ligands.

The Sn(II) derivative was synthesized through the use of an amide-alcohol exchange reaction using $[Sn(NMe_2)_2]_2$ (**1**)[24-26] and HONep (eq 1). The product isolated was the novel polymeric Sn(II) alkoxide, $[Sn(\mu\text{-}ONep)_2]_8$ (**2**) shown in Figure 3. Through ^{119}Sn NMR experiments, the polymeric compound **2** was found to be disrupted into smaller oligomers in solution. The introduction of water (typically through ambient atmospheres) is critical to the formation of the cross-linked M-O-M film network that is necessarily formed during spin-coat

deposition processes. Titration of **2** with H_2O led to the identification of two unique hydrolysis products characterized by single crystal X-ray diffraction as $Sn_5(\mu_3\text{-}O)_2(\mu\text{-}ONep)_6$ (**3**) and $Sn_6(\mu_3\text{-}O)_4(\mu\text{-}ONep)_4$ (**4**), see Figure 3 and eq 2.[27] These compounds were further identified by multi-nuclear (^1H, ^{13}C, ^{17}O, and ^{119}Sn) solid state MAS and high resolution, solution NMR experiments. Based on these studies, it was determined that while the central core of the solid-state structures of **3** and **4** are retained dynamic ligand exchange leads to more symmetrical molecules in solution. The THME ligated and they hydrolysis products have been published and patented.[28]

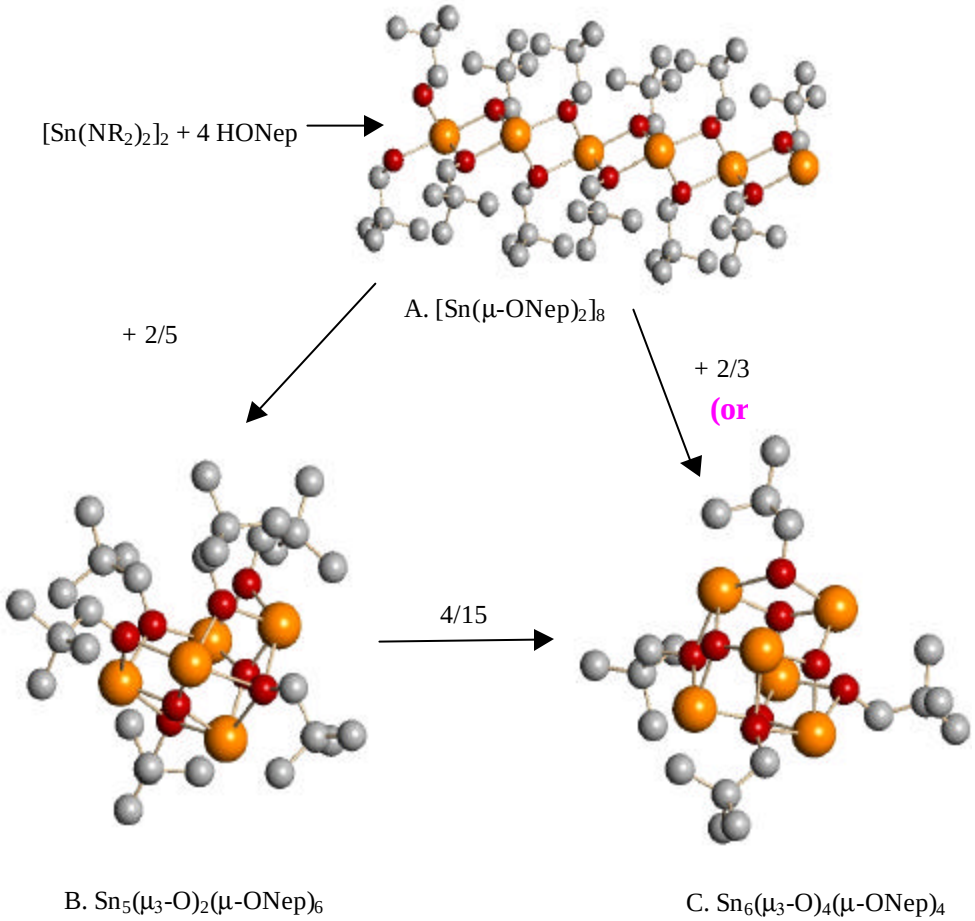

Figure 3. Schematic route to (A) $[Sn(\mu\text{-}ONep)_2]_8$ and its hydrolysis products (B) $Sn_5(\mu_3\text{-}O)_2(\mu\text{-}ONep)_6$ and (C) $Sn_6(\mu_3\text{-}$

$$[Sn(NMe_2)_2]_2 + 4\ HONep \longrightarrow [Sn(ONep)_2]_8 + 4\ HNMe_2 \quad (1)$$

$$[Sn(ONep)_2]_8 + n\ H_2O \longrightarrow "Sn_w(O)_x(ONep)_y" + z\ HONep \quad (2)$$

$$[Sn(ONep)_2]_8 + 4\ HOAc \longrightarrow Sn_6(O)_4(ONep)_4 \quad (3)$$

We also found that **4** could be isolated from the reaction of $Sn(ONep)_2$ with HOAc (eq 3). Due to the simplicity of synthesis and high quality of films generated from this solution it was used as the standard route. A standard synthesis follows for the sol-gel solution. $Sn(ONep)_2$ was slurried in toluene and four equivalents of HOAc were added via pipette. A simple scheme is shown in Figure 4. Typically, 3 layers were deposited and the final film fired at 650 °C. The mixture was stirred for an hour and films were deposited as previously

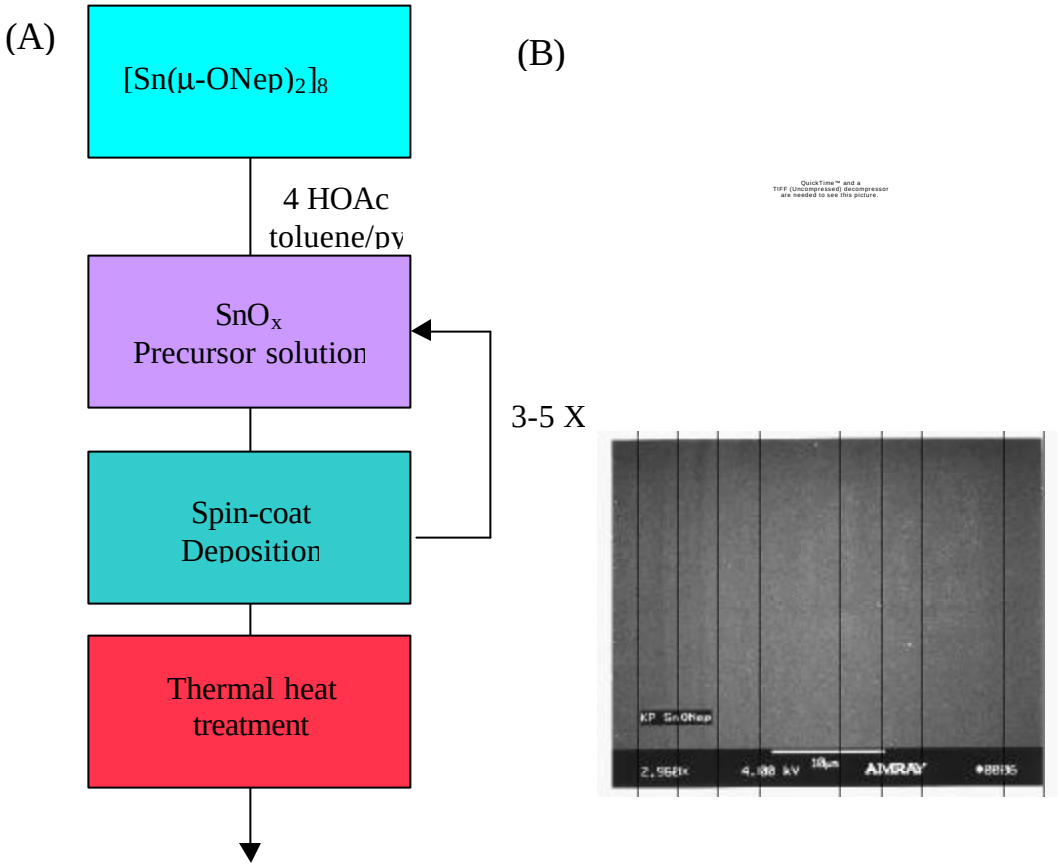

Figure 4. (A) Flow chart and (B) SEM micrographs of the resultant spin-cast deposited films of the anode SnO_x.

described.[29,30] The films generated were found to be extremely uniform and defect free by SEM analysis. Some micrographs of the resultant films are shown in Figure 4. XRD analysis of the film showed that the major phase was cassiterite (SnO_2).

Electrochemical properties. The film properties were evaluated using previously reported methods. The films demonstrate a oxidation/reduction (redox) waves, but on the first cycle the material becomes electrochemically inactive. Figure 5 shows the first and second cycles of the final films. XRD analyses indicates that the film had been converted from SnO_2 to Sn°, and this is shown in Figure 6. While this is not an ideal situation, the resultant material will function as a reversible anode through the reversible formation of a Li alloy on charge/discharge.. To circumvent this situation in the early ACB device, we placed Sn° spots on the substrate by sputtering through a mask. We also developed several methods for generating SnO_2 spots using a mask for the sol-gel routes.

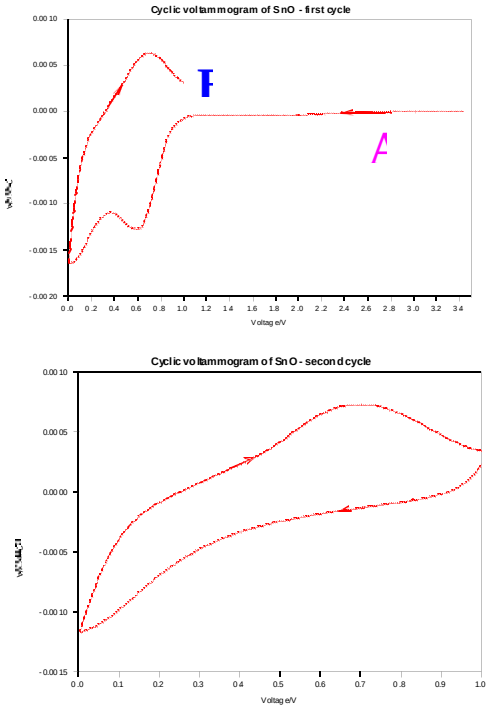

Figure 5. Cyclic voltammagrams of SnO_x thin films.

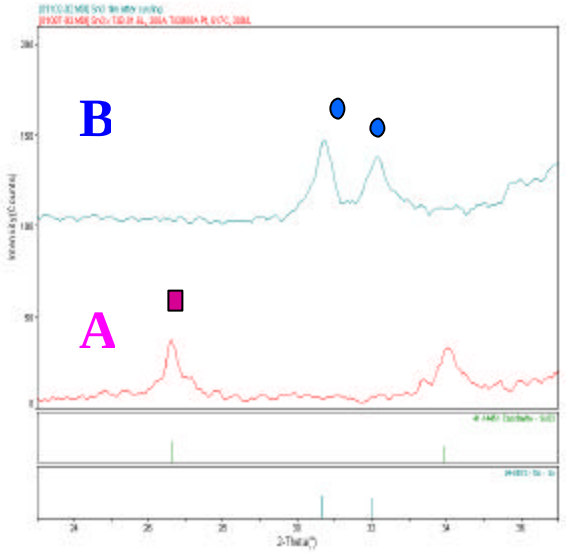

SnO_2,

Sn

Figure 6. XRD of film (A) before and (B) after cycling. Correlates to labels in Figure 5.

5. Cathode.

Currently, several oxides are being considered for use as 4 V cathode materials for Li batteries. These include the spinel $LiMn_2O_4$ and the layered oxides $LiMO_2$ (M = Co and/or Ni).[2-5,31-36] Each of these cathode materials has advantages and disadvantages that impact their further development for lithium-ion batteries.[1-5,31,33,36-46] For example, the capacity of the Mn material is low in comparison to the layered oxide materials, and in the case of the Ni-based oxides the synthesis of high-quality materials is problematic. For these and other reasons, $LiCoO_2$is often the material of choice for use as the cathode in Li-ion batteries. For this activity we too have focused on $LiCoO_2$ as the cathode material for the thin films batteries.

In our system the cobalt oxide was intended as the first layer in the assembly. Furthermore, $LiCoO_2$ is an anisotropic material having a layered structure through which Li^+ moves during charge/discharge to ensure electroneutrality of the film. Consequently, the edge planes of the oxide must be accessible to the electrolyte, and in the solid-state layered system envisioned here, this necessitates formation of the oxide film in a preferred orientation. Hence, several experiments were undertaken to match the lattice of the metal support with the $LiCoO_2$ materials. While Au° appeared to be the best match, after several attempts using both sol-gel and sputtered $LiCoO_2$, oriented materials could not be realized. Therefore, standard stacks using Si/SiO_2//Pt were used. Following is a description of the sol-gels used for the preparation of the cathode materials.

Synthesis/characterization. There are no suitable $Co(OR)_2$ available commercially.[47] Therefore several synthetic routes were attempted to generate the precursor solution. Initially an all amide route was chosen

$$\mathbf{Li(NR_2) + Co(NR_2)_2 \longrightarrow LiCo(NR_2)_3} \quad \mathbf{(4)}$$

$$\mathbf{2\ LiNR_2 + CoCl_2 \longrightarrow Co(NR_2)_2 + 2\ LiCl} \quad \mathbf{(5)}$$

to generate the thin films (eq 4). $Li(NR_2)$ (R = $SiMe_3$) is commercially available and $Co(NR_2)_2$ was synthesized according to eq 5. Films generated from these solutions did not form uniform films. Therefore an all alkoxide route was investigated; however, the precursors investigated demonstrated limited solubility (eq 6 and7).

$$\mathbf{Co(NR_2)_2 + 2\ HOR \longrightarrow "Co(OR)_2"} \quad \mathbf{(6)}$$

$$\mathbf{Li(OR) + Co(OR)_2 \longrightarrow LiCo(OR)_3} \quad \mathbf{(7)}$$

$$\mathbf{Li(ONep) + Co(NR_2)_2 \longrightarrow LiCo(NR_2)_2(ONep)} \quad \mathbf{(8)}$$

$$\mathbf{Li(ONep) + Co(NR_2)_2 + 2\ HONep \longrightarrow LiCo(ONep)_3} \quad \mathbf{(9)}$$

$$8\ Li(N(SiMe_3)) + 8\ HONep \xrightarrow{tol}$$

Mixing the two approaches (eq 8) yielded films that were powdery in appearance but could be electrochemically investigated. $[Li(ONep)]_8$ was a novel compound synthesized and characterized during this project (Figure 7).[48] Of the characterized Li(OR), this derivative

$[Li(ONep)]_8$

Figure 7. Ball and Stick diagram of $[Li(ONep)]_8$

possesses enough solubility to be useable in sol-gel processes. It was reasoned that the amide would mix with this compound and therefore generate a sol that was useful for film production (eq 9). Further studies showed that an *in-situ* conversion to the alkoxide also yielded high quality films. The majority of films prepared this way were powdery and did not represent robust films but more likely were powders of $LiCoO_2$. A schematic of the preparation and the SEM and AFM of these films are shown in Figure 8.

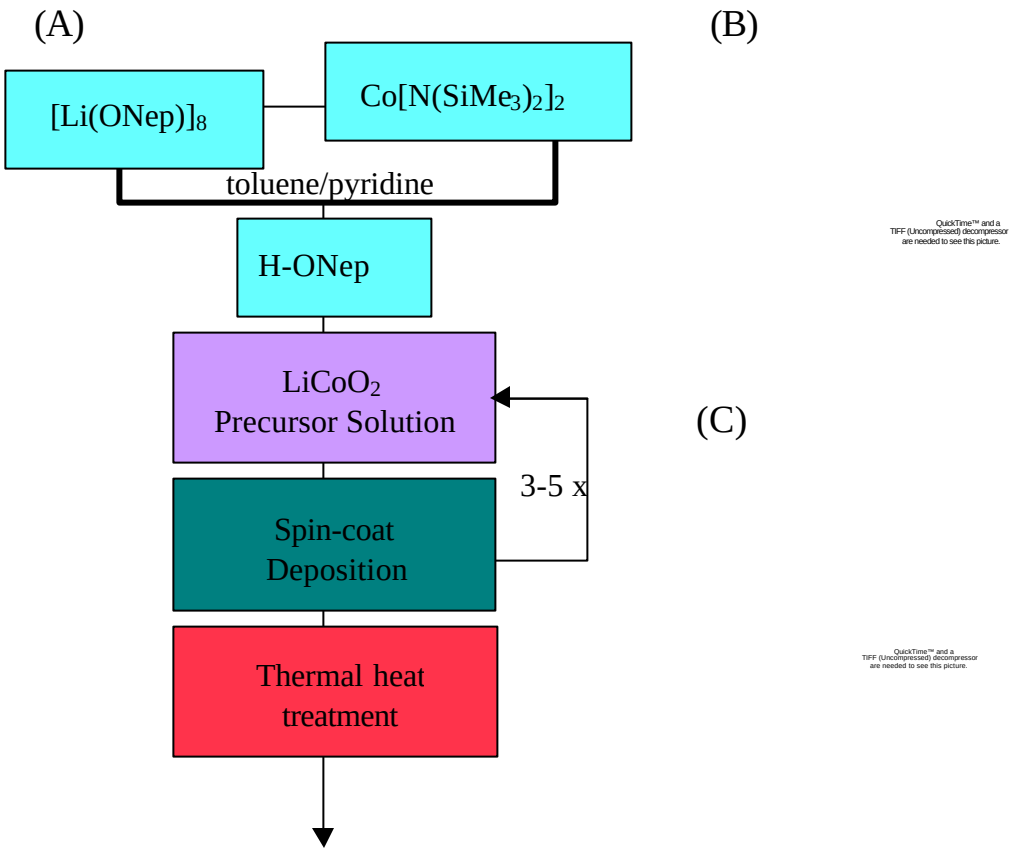

Figure 8. (A) Flow chart and (B) SEM, and (C) AFM micrographs of the resultant spin-cast deposited films of the cathode $LiCoO_2$.

These films were generated during the dry months of winter. Upon the arrival of summer and the use of a "swamp cooler" to chill the air in the laboratory (i.e., higher humidity environment), the above methods failed to produce useable films! This failure was attributed to the increased water content in the atmosphere. In order to circumvent this problem, we switched to another sol that was reminiscent of previous methods used to generate perovskite materials.

$$\mathbf{Li(ONep) + Co(OAc)_2{\bullet}H_2O \longrightarrow LiCo(OAc)_2(ONep)} \qquad \mathbf{(10)}$$

The commercially available $Co(OAc)_2{\bullet}H_2O$ was used by dissolving it in pyridine, Figure 9 and eq 10. Again, the LiONep was used due to its high solubility. Using this method (eq 7) it was possible to generate acceptable films.

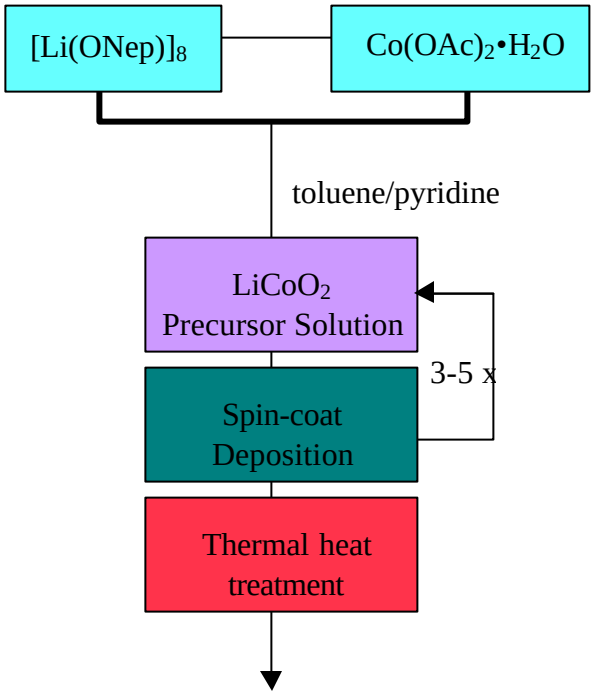

Figure 9. Flow chart of alternative route to $LiCoO_2$.

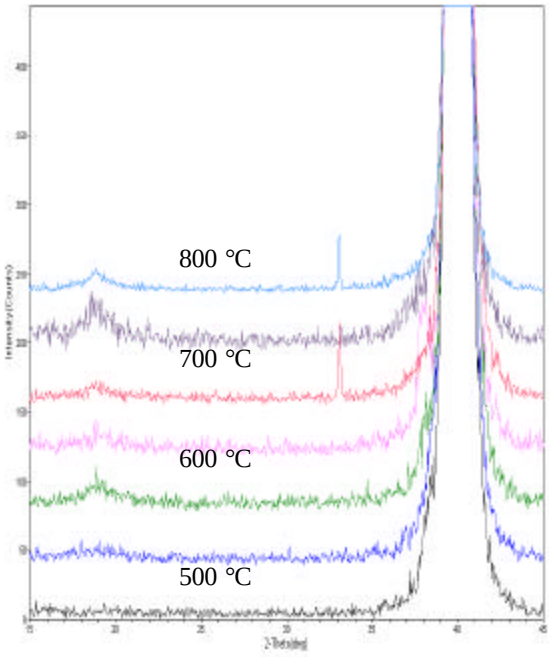

Figure 10. XRD of $LiCoO_2$ thin films at different temperatures.

This was the sol ultimately used for the remainder of the project due to its robust nature in the face of variable environmental conditions (i.e., variable humidity due to seasonal fluctuations). The various structural changes noted in the film over processing temperature were followed by XRD and are shown in Figure 10. In this figure we see the formation of the textured $LiCoO_2$ film illustrated by the small peak at ~18.5 ^{o} 2θ. This broad peak starts to form at ~600 ^{o}C and is clearly detectable at 800^{o}C. Additional peaks (above 30 ^{o} 2θ) in the patterns are from the Pt electrode and Si substrate. In an effort to simplify the process we also investigated the potential development of a single source precursor (*vide infra*).

Electrochemical properties. A sample that proved to be electrochemically active was studied by XRD throughout the process. The various structural rearrangements that were noted are discussed below. The electrochemical properties of these films were investigated using previously reported methods.[45] The cyclic voltammagrams are shown in Figure 11. Some of the unusual properties were studied in more depth.

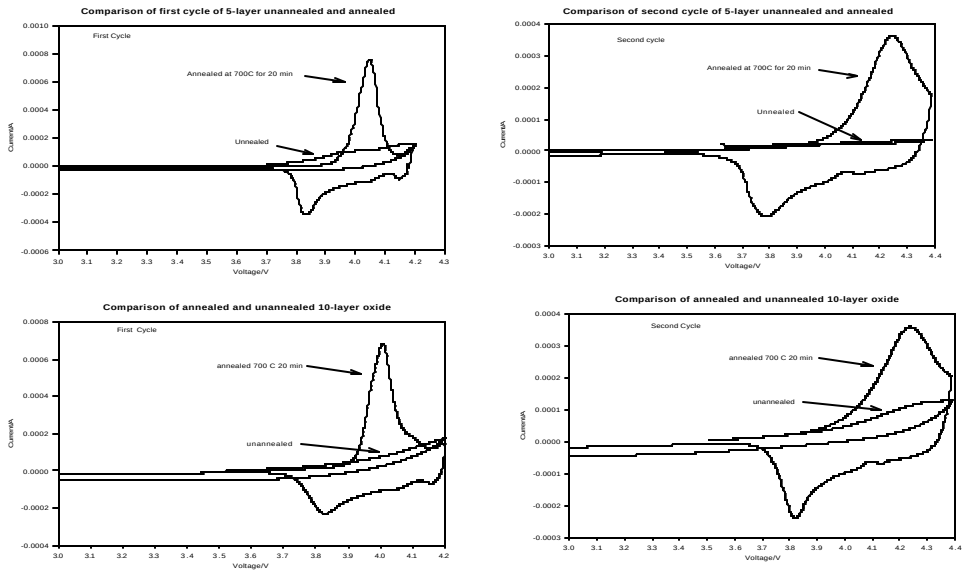

Figure 11. Cyclic voltammagrams of thin films of $LiCoO_2$.

Figure 12 shows the first cycle of the films generated in this process. Figure 13 shows the diffraction data for the $LiCoO_2$ films at various stages of discharge. The "before anneal" film showed very little crystallization behavior (as expected); this is seen by the lack any peak intensity at ~18.5 ^{o} 2θ. Diffraction patterns for the rest of the samples looked essentially the same qualitatively. However, there are some subtle details that could give some structural insight as to what is happening in these films. Specifically, the 2θ region of 17-21 ^{o} 2θ shows a peak doublet for all the annealed films but there are some changes to these peak positions depending on the electrochemical conditions.

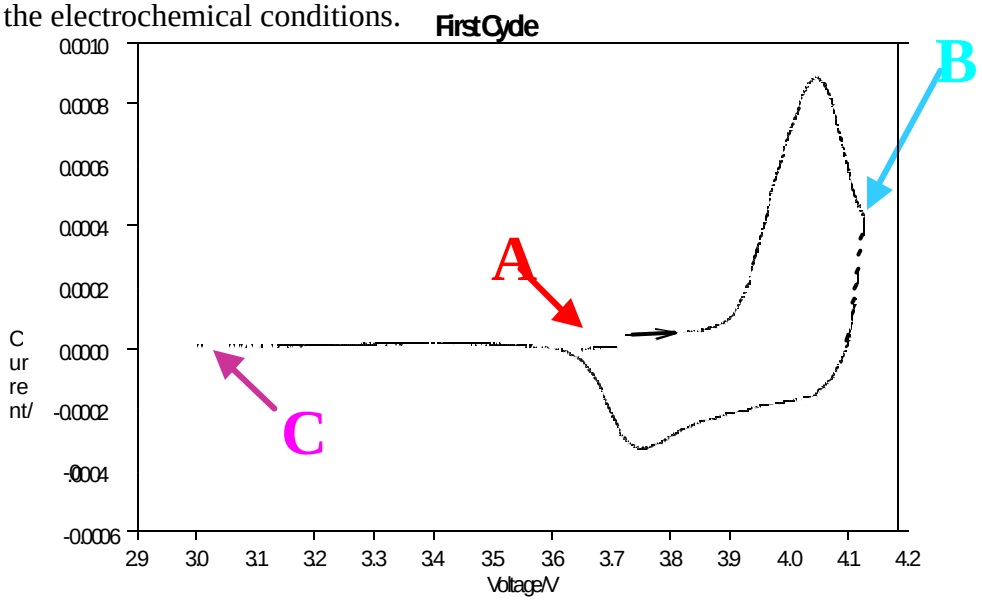

Figure 12. Cyclic Voltammagram for 10 layer $LiCoO_2$ film annealed at 700 °C for 25 min.

Figure 13 shows a zoomed region for three films, annealed, oxidation only, and after one cycle. As one can see, the high angle peak at 18.910 ^{o}2θ (i.e., 2nd peak) shifts to lower 2θ (higher d-spacing) during the oxidation. This behavior is consistent with the shifting of the $LiCoO_2$ (003) peak during charging that we have observed in our powder cathodes. The low

angle peak (i.e., 1st peak) only shifts slightly during the oxidation (+0.018 °), while the 2nd peak shifts more

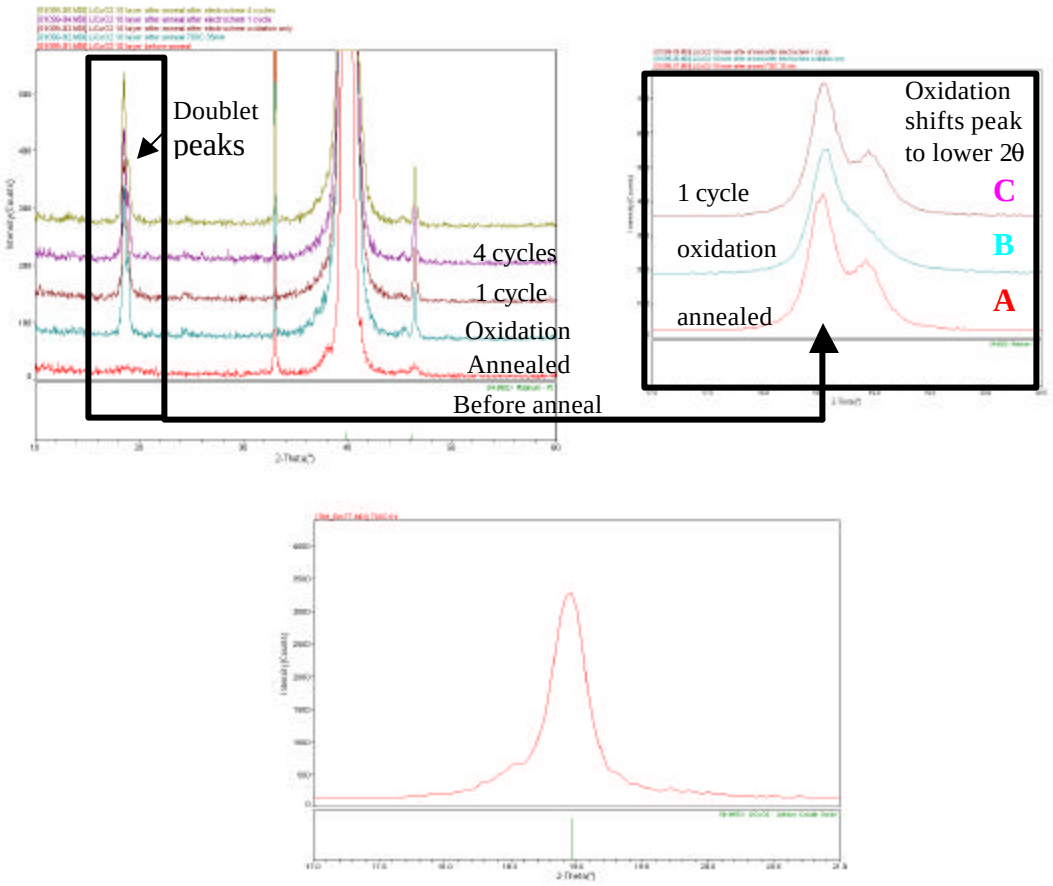

Figure 13. XRD pattern of $LiCoO_2$ films during cycling.
The A, B, C correlate to Figure 12 labels.

Table 1. Profile fit results for peak doublet in 17-21 °2q region.

	1st peak				2nd peak			
Sample	d (Å)	2θ (°)	$LiCoO_2$ c-axis (Å)	FWHM (°)	d (Å)	2θ (°)	$LiCoO_2$ c-axis (Å)	FWHM (°)
anneal	4.7929	18.497	14.379	0.266	4.6890	18.910	14.067	0.280
oxidation	4.7882	18.515	14.365	0.277	4.7017	18.858	14.105	0.423

1 cycle	4.7891	18.512	14.367	0.275	4.6801	18.946	14.040	0.283
4 cycles	4.7909	18.504	14.373	0.262	4.6816	18.940	14.045	0.310

significantly (-0.052 ^{o}). After one cycle, the 1st peak stays essentially fixed while the 2nd peak shifts to higher 2θ (+0.088 ^{o}) resulting in a peak at higher 2θ than the original annealed sample (18.946 ^{o}). Table 1 shows the profile fit results for peak positions of the doublet. The significant increase in the FWHM of the 2nd peak during oxidation is also notable. The FWHM value returns to a smaller value upon reduction. This increase in FWHM is likely due to microstrain in the sample, as it is not likely that the crystallite size is changing during cycling and the electrochemical process of Li de-intercalation is likely to cause some stress in the film. The 1st peak FWHM stays relatively constant through the cycling. Quantified profile fit results for the film after four cycles are essentially the same as that of the one cycle sample.

After evaluating the peak positions determined in the films, it seems plausible that the 1st peak likely results from a highly Li deficient $LiCoO_2$ (003) peak having a c-axis in the range of 14.365 – 14.379 Å (see Table 1). This c-axis range is typical of de-lithiated Li_xCoO_2 (x ~ 0.3) that we have observed in $LiCoO_2$ powders. The 2nd peak is consistent with a (003) reflection from a high Li content $LiCoO_2$ having a c-axis in the range of 14.040 – 14.067 Å in the discharged state. This range is fairly typical of a fully lithiated $LiCoO_2$ sample from powder measurements.

In general from these films, it was determined that the films were re-cycleable in the battery sense and were smooth enough to be the base of the ACB.

Single source $LiCo(OAr)_4(solv)$.[47] In search for a single source precursor, several reactions were investigated. Of these, the reaction between $LiN(SiMe_3)_2$ and $Co(N(SiMe_3)_2)_2$ in THF followed by the addition of an aryl alcohol (HOAr) yielded $Li_2Co(OAr)_4(THF)_x$: $Co[(\mu\text{-}OAr)_2Li(THF)_x]_2$ [where x = 2: OAr =: OC_6H_4Me-2, (oMP, **1**, shown in Figure 14), $OC_6H_4(OCHMe_2)$-2 (oPP, **2**),

$OC_6H_3(Me)_2$-2,6 (DMP, **3**); where x = 1: OAr = $OC_6H_3(OCHMe_2)_2$-2,6 (DIP, **4**)] which proved to

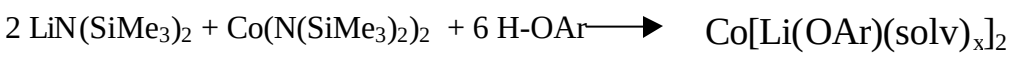

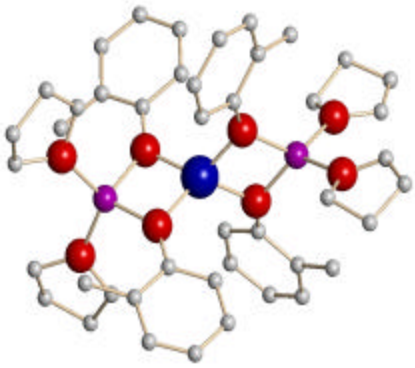

oMP

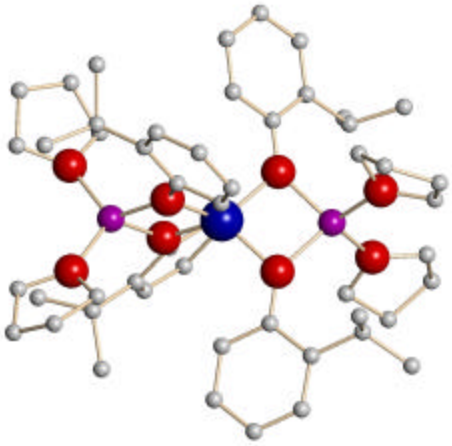

oPP

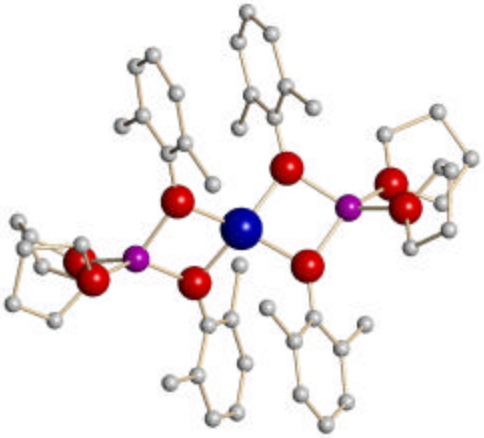

DMP

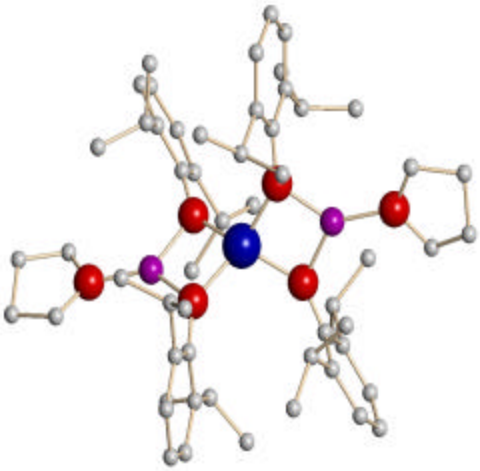

DIP

Figure 14. Synthesis and crystal structure of novel family of $Co[Li(OAr)(solv)_x]_2$ compounds.

have the qualities necessary to be useful as a single source precursor. Thin films of the spinel phase of $LiCoO_2$ were formed by spin-cast deposition methods using **5** or **6** dissolved in a pyridine/toluene mixture onto platinized silicon wafers followed by firing at 700 °C, see Figure 15. Cyclic voltammetry revealed two irreversible oxidation processes followed by one reversible process, the latter of which is found to occur at about 4.2 V and is shown in Figure 16. XRD analysis of the thin film, both before and after electrochemical cycling, revealed only minimal variations in the crystal structure of the film after cycling (see Figure 16). This family ofcompounds, even though stoichiometrically incorrect, have been shown to be useful for single source applications in the solid and liquid techniques.

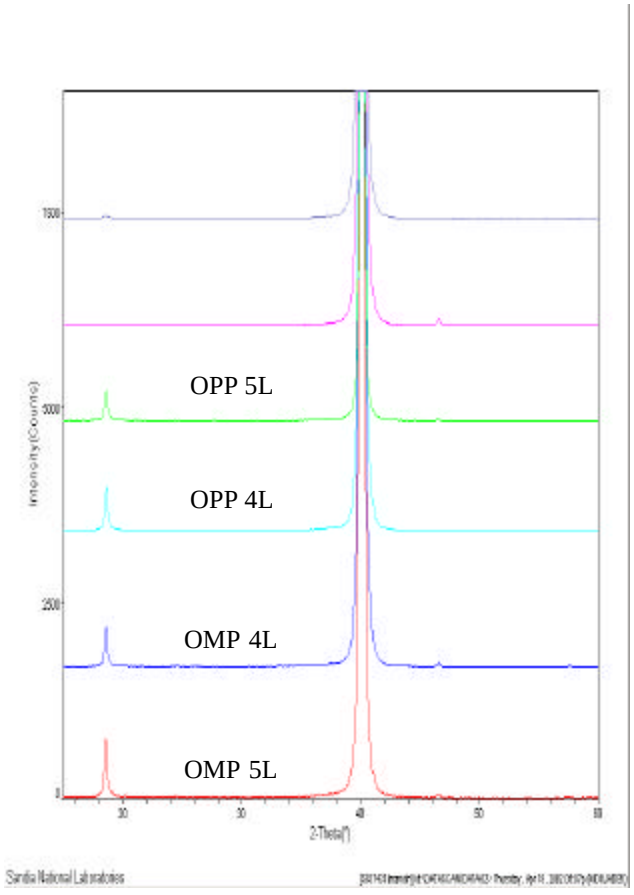

Figure 15. XRD patterns of $LiCoO_2$ thin films from oMP and oPP at different thicknesses.

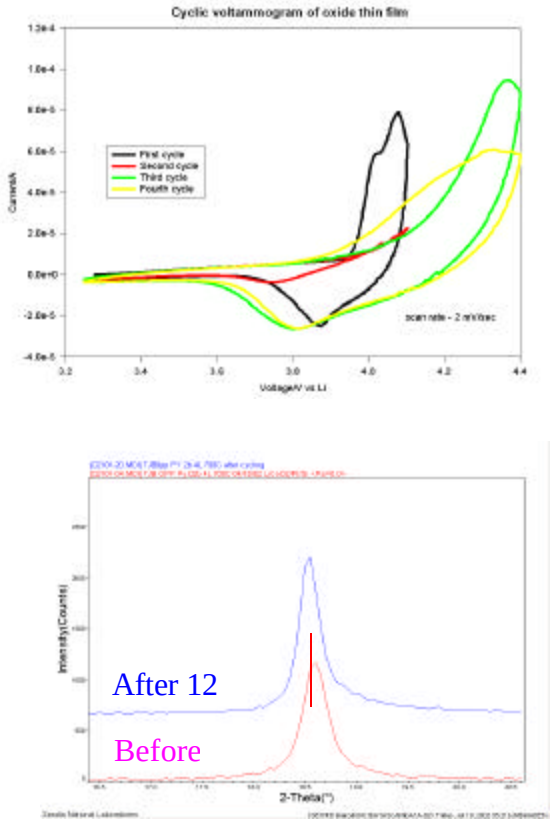

Figure 16. (A) Cyclic voltammagram of thin film of $LiCoO_2$. (B) XRD of film before and after cycling. The film is in the discharged state in both cases.

6. Electrolyte

Two approaches were undertaken to generate the electrolyte for the ACB. The first was to generate a solid state ceramic electrolyte. In parallel, the synthesis of a thin film PEG block co-polymer electrolyte was also investigated. These are discussed separately below.

A. Ceramic. Our initial choice for an electrolyte was to use a modified glass involving the $LiLnPO_3$ where Ln = the lanthanide series and yttrium. Solutions were made by the dissolution of the nitrate (NO_2) derivatives in water followed by phosphoration using phosphoric acid. Drying and processing at 900 °C converted these sols to a phase pure material. However, these materials proved to be only soluble in phosphoric acid. Unfortunately, this sol dissolved the $LiCoO_2$ and SnO_2, the very layers that it would need to be deposited onto. Testing of a pressed pellet showed low conductivity; however, a rigorous test was not performed and these materials may have acceptable Li conductivity. Combined, these data suggest that alternative materials should be investigated. Several literature reports suggest that (Li,La)TiO_3 (LLT) perovskite materials had high Li-conductivities at room temperature (Figure 17).[49-51]

Synthesis/Characterization. The synthesis of the LLT solution involved specialty chemicals developed in our laboratory. Once again, $[Li(ONep)]_8$[48] (Figure 7) was used for the alkali metal precursor, $[Ti(\mu\text{-}ONep)(ONep)_3]_2$[52] (Figure 18) was used for the group IV source, and the literature complex $La(DIP)_3(py)_2$[53] (Figure 18) was used as the lanthanide precursor (eq 11).

$$\mathbf{1/8\ [Li(ONep)]_8 + 1/2\ [Ti(\mu\text{-}ONep)(ONep)_3]_2 + 2\ La(DIP)_3(py)_2 \xrightarrow{D} LLT} \quad (11)$$

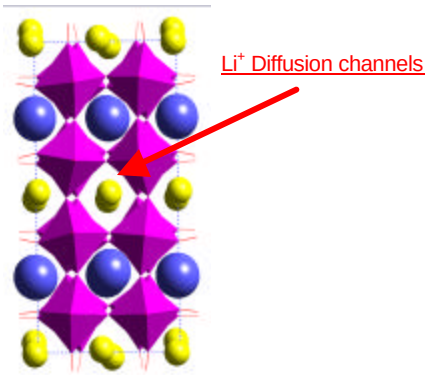

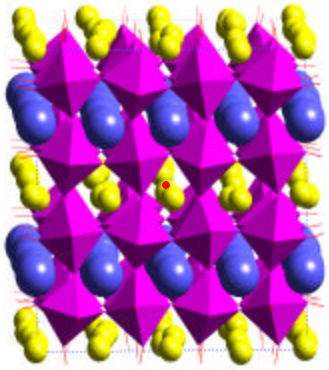

$La_{1/2}Li_{1/2}TiO_3$

$La_{33}Li_{29}\square_2Ti_{64}O_{192}$

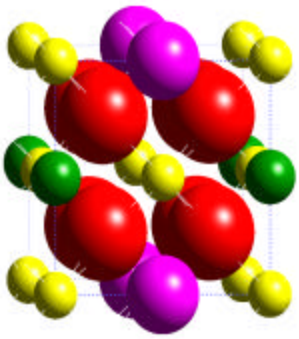

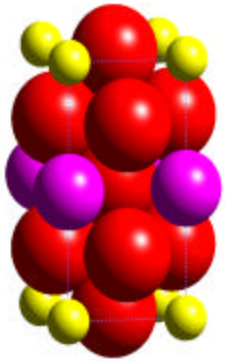

Fluorite

Perovskite

Figure 17. Computational models of the electrolyte LLT.

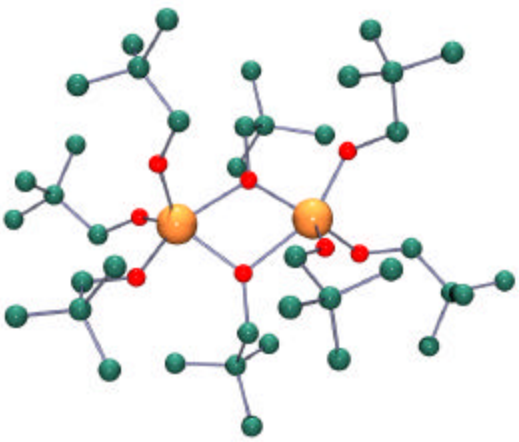

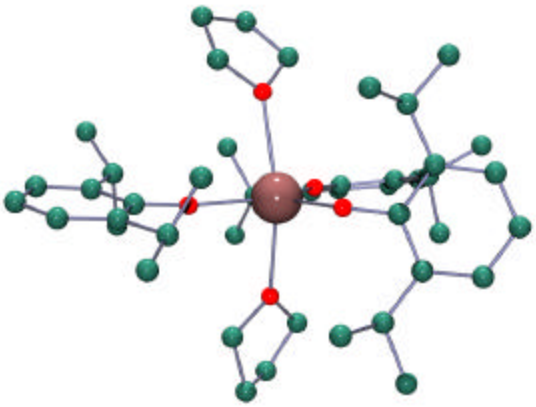

$[Ti(\mu\text{-}ONep)(ONep)_3]_2$

$La(DIP)_3(THF)_3$

(py structure is reportedly analgous)

Figure 18. Ball and Stick diagrams of LLT precursors.

These were combined in pyridine and toluene. High quality thin films were generated and characterized by SEM (Figure 19); however, standard processing did not yield the desired perovskite phase but instead a fluorite phase was isolated. Additional heating did not alter the phase. Therefore rapid thermal heat treatment protocols were undertaken and the perovskite phase was observed by XRD analysis (see Figure 20).

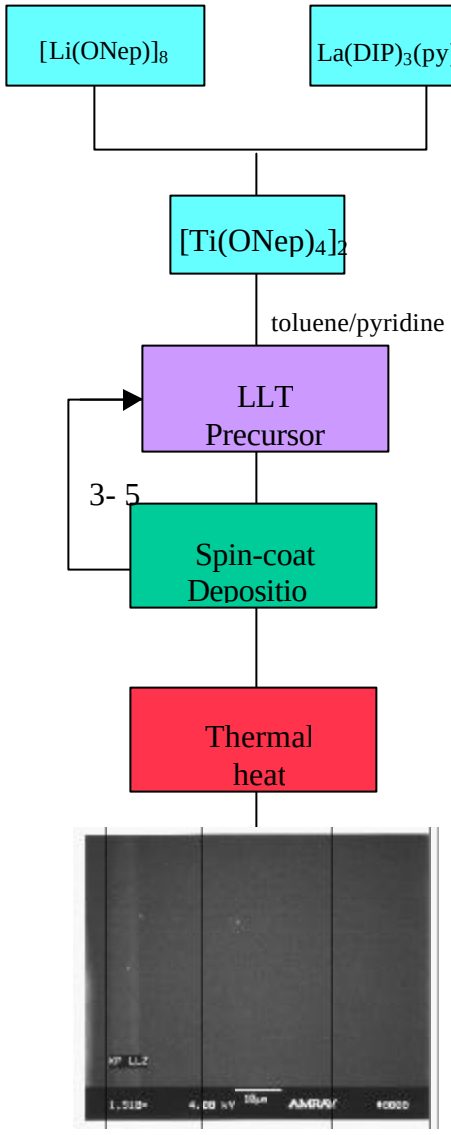

Figure 19. (A) Flow chart and (B) SEM micrographs Of the resultant spin-cast deposited films of the cathode $LiCoO_2$.

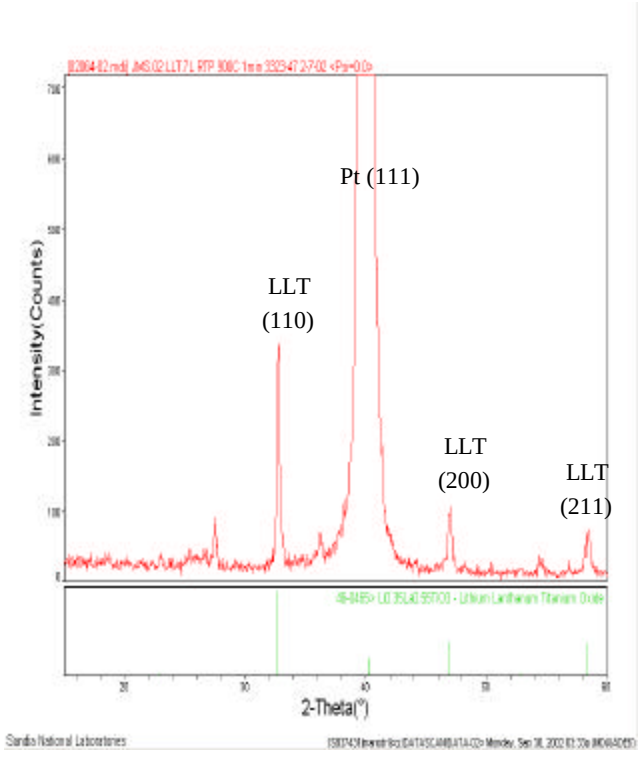

Figure 20. XRD pattern of perovskite LLT thin film.

Additional Group IV and V modifiers were also added to this mix to improve the stability of the final material. These included $[Zr(OPr^i)(ONep)_3(HONep)]_2$,[54] $[Nb(\mu\text{-}OEt)(ONep)_5]_2$,[55] and $[Ta(\mu\text{-}OEt)(ONep)_5]_2$[54] to form $LiLaZrO_3$ (LLZ), $LiLaNbO_3$ (LLNb), and $LiLaTaO_3$ (LLTa), respectively. It was difficult to make high quality perovskite films of these additional dopants. LLZ requires much higher and longer crystallization times, LLNb and LLTa both formed the proper phase but the films possessed very rough features after processing and were difficult to obtain phase pure. With the use of rapid thermal treatment, it was possible to synthesize nearly phase pure perovskite LLT films. Therefore, LLT was selected as the material of interest. All of the LLT films produced to date have shown to be shorted, independent of the thickness of the film.

B. Polymer. The approach undertaken for the polymer electrolyte was to utilize thin film ion-conducting ORMOLYTES[9,10] containing lithium ions. Figure 21 shows a schematic representation of the functionality of these films. Two approaches were followed for these films. The first approach was to utilize a mixture of tetraethoxysilane (TEOS) as the inorganic phase and polyethyleneglycol (PEG) as the organic phase with various lithium salts. In this type of mixture the inorganic and organic phases of the ORMOLYTE are simply physically mixed with each other and there are no chemical bonds present between them. Once the mixtures

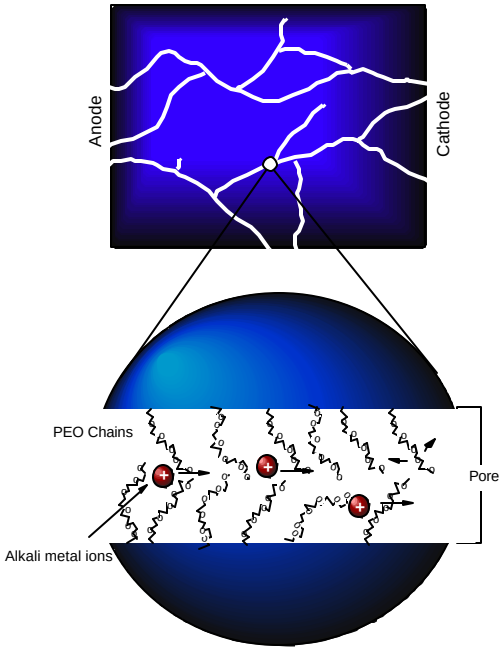

Figure 21. Schematic diagram of the functionality of the ORMOLYTE films.

were made, they solution was spin coated onto substrates in order to study the quality of the deposited film. Several solvents as well as neat solution, lithium salts and PEG of varying molecular weights were used. Unfortunately, no combination afforded uniform films of good quality. In many cases, crystallization and/or de-wetting were observed once the film was spin coated onto the test substrate (silicon). Therefore, the second approach, where there is a chemical bond present between the inorganic and organic phase, was undertaken.

The mixture that contains chemical bonds between the inorganic and organic phases of the ORMOLYTE was prepared according to eq 12.

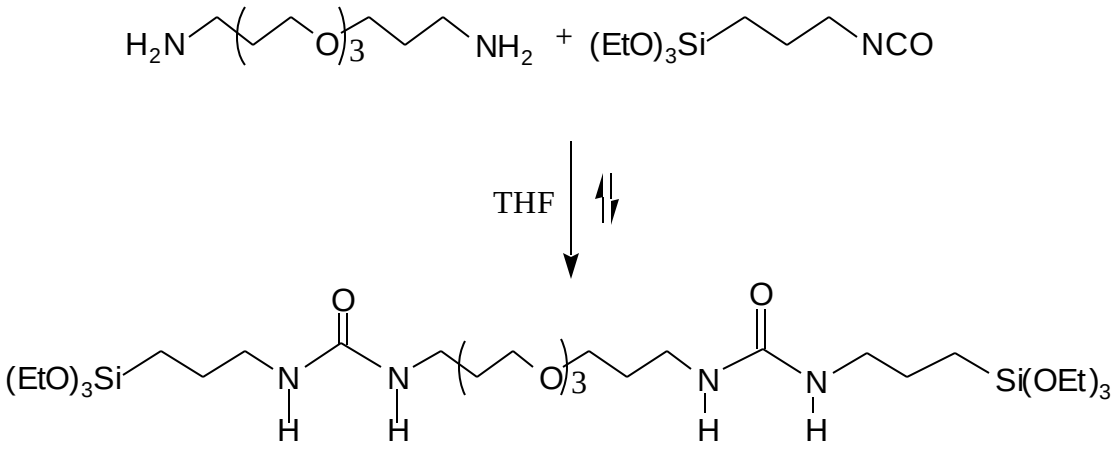

(12)

The mixture of the amine and the alkoxysilylisocyanate was refluxed in tetrahydrofuran (THF) and after removal of the solvent (THF), the product was left behind as a thick oil. This oil was then dissolved in ethanol, ammonium fluoride (NH_4F) catalyst was added, followed by the lithium salt and water, necessary for the hydrolysis and condensation of the alkoxide functionalities. This homogeneous mixture was then stirred for approximately 20 minutes to insure the initiation of the sol-gel reaction before it was spin coated onto the substrate. Several lithium salts were tested for this process and it was found that lithium perchlorate and lithium

triflate gave the best results. After spin coating, the films were cured at 90 °C for about 96 hours to insure completion of the sol-gel reaction as well as removal of any of the volatile species present, namely ethanol.

Films of these materials were cast onto a gold film deposited onto a silicon wafer. This gold layer then served as the electrical contact to one side of the film. After preparation of sample film on the gold layer, small gold circular deposits having a diameter of 0.25-inches were then placed on top of the sample film, thereby sandwiching the sample between two gold layers, the bottom layer covering the entire substrate and the 0.25-inch gold spots. These gold layers served as blocking electrodes for making all conductivity measurements. Prior to making impedance measurements, DC resistance measurements of the samples were made to ensure that the electrodes were not electrically shorted. This initial measurement also provided a gross, indirect measure of the integrity of the film. In virtually every case the films received were electrically shorted. Efforts were then made to improve the mechanical characteristics of these films, and these activities came to fruition in the form of six samples that were not electrically shorted. Impedance measurements of these films were then made in a frequency range of between 100 kHz to 1 mHz and in every case the ionic conductivity was found to be very low (reliable data could not be obtained due to the limitations of the instrumentation.) Since only six samples were evaluated using this approach, additional work should be performed in order to fully assess this approach for the preparation of ionically conductive thin films.

7. General Molecular Modeling

Molecular simulation techniques were initially used to examine the various structures of several components (substrate, conductor, anode, cathode, and electrolyte) of the ACB device.

The theoretical approach was useful for evaluating candidate materials, especially those to be used as the electrolyte for which a high ionic mobility was required. Molecular modeling methods provide a relatively fast and inexpensive route to evaluating candidate materials and determining optimal improvements in structure to enhance material performance. We built upon our previous success in the molecular simulation of spinel-based cathode materials[56,57] and extended the work to examine the behavior of layered cathodes and electrolytes to be used in the thin film ACB. Initial work examined the topological relationship between cathode and conductor based on forcefield energy calculations of the fit-mismatch associated with the registry of the materials ($LiCoO_2$ and Pt or Au) at an interface. The need for a fast ion conductor material for the electrolyte part of the ACB device was addressed by examining the structures of various phosphate, aluminate, silicate, vanadate, and titanate structures. Ultimately, molecular simulations of the lanthanum lithium titanate phases were performed to evaluate compositional and structural effects on the transport of lithium. The candidate phosphate materials were abandoned due to stability concerns and materials compatibility issues.

A. Cathode and Metal Conductor Compatibility. Strain energies with respect to various crystal planes of the $LiCoO_2$ cathode phase were semi-quantitatively estimated based on lattice matching on different surfaces of metal substrates. The greater the mismatch, the greater strain energy and the less favorable the relative orientation. The metals considered were platinum and gold, with particular emphasis on those surfaces providing the best match of lattice spacing with the optimum (101) and (104) $LiCoO_2$ surfaces. An examination of the layered cathode structure[58] (see Figure 22) indicates that the most efficient pathway for charge transfer from the conducting substrate to the layered cathode will be along the orientations having the lithium

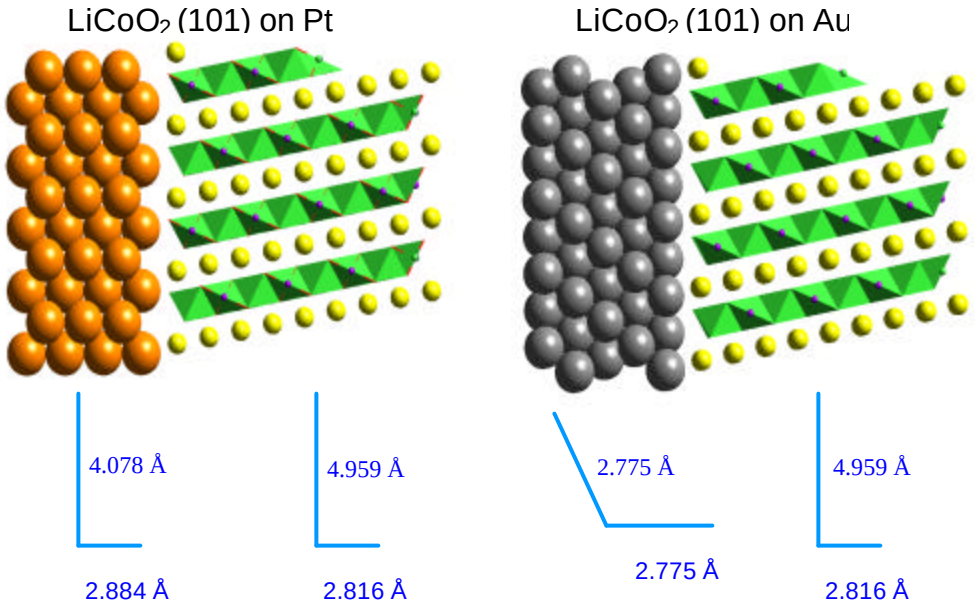

Figure 22. Schematic model of the layered oxide structure.

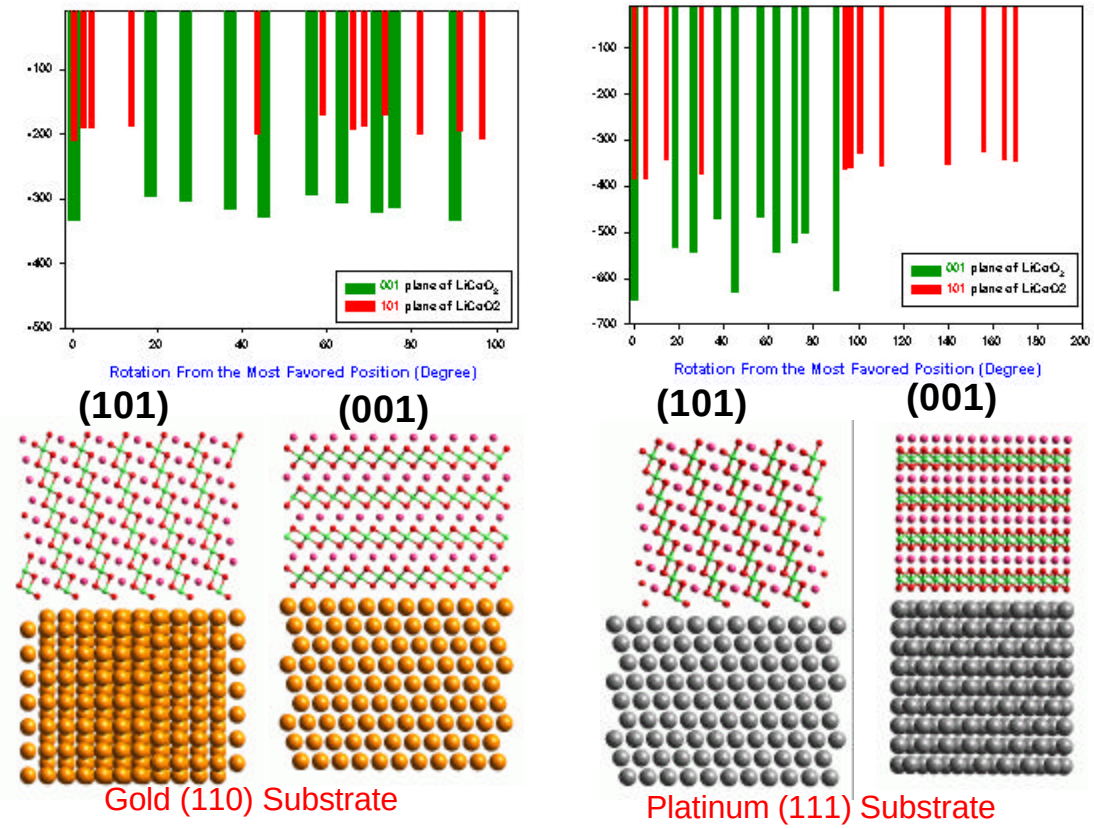

Figure 23. Computation models of the configurations for match between oxide and metal.

layers aligned most normal to the metal substrate (i.e., the (101) and (104) surfaces), thereby allowing the lithium charge carriers to have high mobility through the cathode and electrolyte to the anode of the ACB device.[59] Molecular models of the two metals and layered cathode were generated and assigned forcefield and parameters and partial charges based on the universal forcefield of Rappé et al[60] and Rappé and Goddard[60], respectively. No atomic relaxation was allowed, thereby maintaining the atoms at their crystallographic positions.

The configurations for the most favored match between oxide and metal are presented in Figure 23. The best match was found between the $LiCoO_2$ (101) surface and the gold (110) surface where the overall lattice mismatch is less than 2.3%. The best match found for the (101) surface of the layered oxide on platinum was determined to be the Pt (111) plane with a mismatch of less than 3.1%. The strain energy for these interfaces is related to the volume strain, assuming bulk unit cell parameters, that dominates the interface interactions when the thin film thickness is greater than one micron. As the ACB device incorporates relatively thin cathode films (on the order of 4000 Å) surface energy effects will be more important,[59,61] and therefore requiring full relaxation. Subsequent analysis examined the variation of interaction energy as a function of interface rotation angle. Results are presented in Figure 23. The changes in energy suggest the preferred association of the cathode (001) surface with the both the gold (110) and platinum (111) surfaces. The more efficient lithium-ion transport orientation, the $LiCoO_2$ (101) surface, is significantly less stable for all rotation angles.

This result indicates the difficulty of creating optimum thin film orientations for batteries when thicknesses as low as 500 Å are strongly controlled by surface energies. Batesand co-workers[59] demonstrated this behavior for their sputtered films where at small thicknesses the (001) orientation of the cathode dominates on an alumina substrate. Ultimately, our

experimental efforts were met with limited success in matching the cathode lattice to the metal substrates with both sputtered and sol-gel synthesis methods. We resorted to using the standard thin film substrates comprised of silicon-silicon oxide-platinum stacks that eventually provided a successful substrate for the polycrystalline cathode material.

B. Electrolyte Materials. A literature search was performed to identify potential oxide-based ceramic materials that would be beneficial to the transport of lithium ions through an open structure characterized by channels or layering, while remaining inert and having a low dielectric constant and electrically insulating properties. The crystal structures of several top candidate structures were obtained and examined graphically. These include the perovskite structure $LaLiTi_2O_6$ (see Figure 17),[62] layered perovskite $LiLaNb_2O_7$;[63] nehpheline $LiAlSiO_4$,[64] anti-fluorite Li_4LaTiO_4 (see Figure 17),[65] monazite $Li_{0.9}La_{0.7}VO_4$,[66] and a pseudo-garnet $Li_5La_3Ta_2O_{12}$.[67] Beta-alumina ($Li_8Al_{22}O_{34}$) and beta-double prime alumina ($Li_{24}Al_{33}O_{51}$) structures[68] were also examined. These non-stoichiometric materials are characterized by alternating layers of close-packed oxide having a low density layer containing mobile alkali cations such as lithium.

Not all candidate electrolyte materials were amenable to synthesis using a relatively fast and inexpensive solution route, therefore only a couple of the electrolytes were chosen for molecular modeling and energy calculations. In order to obtain the most desirable electrical conduction at room temperature, the optimal solid-state electrolyte performance requires a high rate of lithium ion mobility through an open crystalline structure. In some solid ion conductors, including phosphates, titanates, and vanadates, lithium ion conductivity has been measured as high at 10^{-3} S/cm at room temperature.[69-71] Inaguma[70] and Bohnke[62] suggested the use of a

perovskite-type structure (ABO_3) with cation deficiency at the A-sites whereby the vacancy defects provide a suitable fast-conducting route favorable for high ionic mobility of lithium ions through four adjacent BO_6 octahedra.

The need for a fast ion conductor material for the electrolyte part of the ACB device was addressed by examining the structures of various phosphate and titanate structures, as noted above. Ultimately, molecular simulations of the lanthanum lithium titanate (LLT) phases were performed to evaluate compositional and structural effects on the transport of lithium. The lithium lanthanum zirconate (LLZ) perovskite was also considered for analysis but was not as easily synthesized compared to the LLT. A similar approach was used to assess the lithium diffusion rate in the nepheline-based electrolyte. The candidate phosphate and materials were abandoned due to stability concerns and materials compatibility issues. Only one previous study has used molecular modeling methods to examine ionic mobility in an ionic conductor. Katsumata and co-workers[72] performed molecular dynamics simulations that suggested lithium diffusion rates at 300 K to be approximately 1.5×10^{-7} to 1.4×10^{-9} cm^2/s depending on the lithium perovskite configuration. However limited diffusion of lithium was observed due to the fairly short simulation times, their use of fixed cell parameters, and perhaps in their manual choice of parameters for the interatomic potentials.[72]

Large-scale molecular dynamics simulations were performed for the $(LaLi)TiO_3$ system in which the La to Li ratio was varied. NPT ensemble dynamics of cells comprised of 320 to 450 atoms were used to assess the relative diffusion rates of Li within the perovskite structure of the titanate. The large simulation cell was generated from the observed perovskite crystal structure[62] by replicating the unit cell to a 4 x 4 x 2 supercell. Atomic trajectories for simulations at 300 K

and 1 atm were obtained for up to 500 psec of simulation time, enough to provide sound statistics on the mobility of the lithium ions. Initial simulations examined the stoichiometric (La/Li = 1) and ordered structure. The introduction of A-site vacancies into the simulation cell with increased La and decreased Li (La/Li > 1) indicated a measurable increase in lithium diffusion rates. The simulations suggest an optimum stoichiometry for the titanate to be approximately La/Li = 3 whereby significant metal vacancies occur while maintaining a high lithium concentration (La = 0.6, Li = 0.2, vacancy = 0.2) for the $(LaLi)TiO_3$ phase. This stoichiometry was later used as a basis for the solution-based synthesis of the thin film electrolyte in the ACB assembly.

Subsequent simulations were refined by the use of new forcefield parameters[73] and by systematically increasing the La and defect concentrations in order to properly identify the optimum composition for the performance of this electrolyte. The new forcefield parameters were derived from density functional theory whereby idealized structures for metal-oxygen interactions were used to parameterize Buckingham potentials. The interaction potential between any two atoms (or ions) is represented by the following energy expression (eq 13):

$$E(r_{ij}) = \frac{z_i z_j e^2}{r_{ij}} + A_{ij}\, exp(-B_{ij} r_{ij}) - \frac{C_{ij}}{r_{ij}^6} \qquad \textbf{(13)}$$

where r_{ij} is the distance of separation between atoms i and j, z_i is the partial charge, e is the charge of an electron, and A_{ij}, B_{ij}, and C_{ij} are empirical parameters for the atom pair. The first term represents the electrostatics or Coulombic interaction and is the dominant component of the crystal internal energy. The second term is a two-parameter Born-Meyer short range repulsion term and the third term represents the short range attractive dispersion (van der Waals)

interaction. An alternative forcefield approach was also used to evaluate the total lattice energy. A commercial forcefield CVFF_aug, based on the functionality of Dauber-Osguthorpe[74] was also used to evaluate the total lattice energy (eq 14):

$$E(r_{ij}) = \frac{z_i z_j e^2}{r_{ij}} + \frac{A_{ij}}{r_{ij}^{12}} - \frac{B_{ij}}{r_{ij}^{6}} \qquad \textbf{(14)}$$

This method uses the standard Lennard-Jones 6-12 potential to represent the short range interactions, and incorporates a single parameter for the repulsion term. Initial bulk structure determinations and optimizations for the LLT and the lithium nepheline structures were obtained with the CVFF_aug potential. This approach was eventually discarded in favor of the Teter[73] parameters and the Buckingham functionality, and which provided well-behaved dynamics simulations. The lithium ion diffusion coefficients derived by each method were similar and typically were within an order-of-magnitude in agreement.

The molecular dynamics simulations were performed with both NVT and NPT canonical ensembles at room temperature (300 K) and 1 atm (NPT only). NVT simulations were eventually abandoned in favor of the NPT dynamics. NPT methods avoid the buildup of forces on the periodic boundary of the simulation cell and therefore are more realistic by having no constraints on the simulation. Therefore, all cell parameters and atomic positions are allowed to vary during the simulation. The system was first allowed to equilibrate over approximately 5 ps of simulation time using a 1 fs time step. Typically, no lithium migration occurred during this initial period. Trajectories for the lithium were obtained for up to 500 ps for each simulation. The excessively long simulation times ensures that the simulation produces a lithium trajectory having diffusion among lithium sites, and that enough site hopping occurs to provide a statistical

basis for deriving diffusion coefficients. Analysis of the mean square displacement of the lithium ions in the structure as a function of time provides (slope is equal to 6*D*; Nernst-Einstein relation) the lithium diffusion coefficient. No lithium diffusion occurs if all A-sites of the perovskite LLT are occupied. However, lithium mobility is observed with the introduction of lithium vacancies and the associated increase in lanthanum content. No migration of the titanium, lanthanum, or oxygen ions was observed in any of the simulations. Lithium diffusion coefficients derived from the LLT simulations range from zero to 5 x 10^{-6} cm^2/s. Increasing the lanthanum content and the corresponding number of A-site vacancies, as noted above, lead to an apparent increase in diffusion coefficient values, although the variation in results did not allow for a statistical correlation. Similar lithium diffusion values were derived for the lithium nepheline (zero to 2 x 10^{-5} cm^2/s) but we make no distinction in the relative values due to the similar range of values obtained for each phase. Ten molecular dynamics simulations were completed for the LLT and four for the nepheline. The simulation cells used in the dynamics runs are presented in Figure 24.

It is apparently sufficient to state that the dynamics simulations demonstrate the capability of the LLT and the Li nepheline to have lithium ions diffuse through the lattice at room temperature conditions, as would be expected for an efficient solid state electrolyte. We did not investigate the influence of temperature on these results. A more detailed set of dynamics simulations is required to clearly define the variation of diffusion coefficient with defect concentration, and to derive activation energies for lithium diffusion by performing the simulations at several higher temperatures.

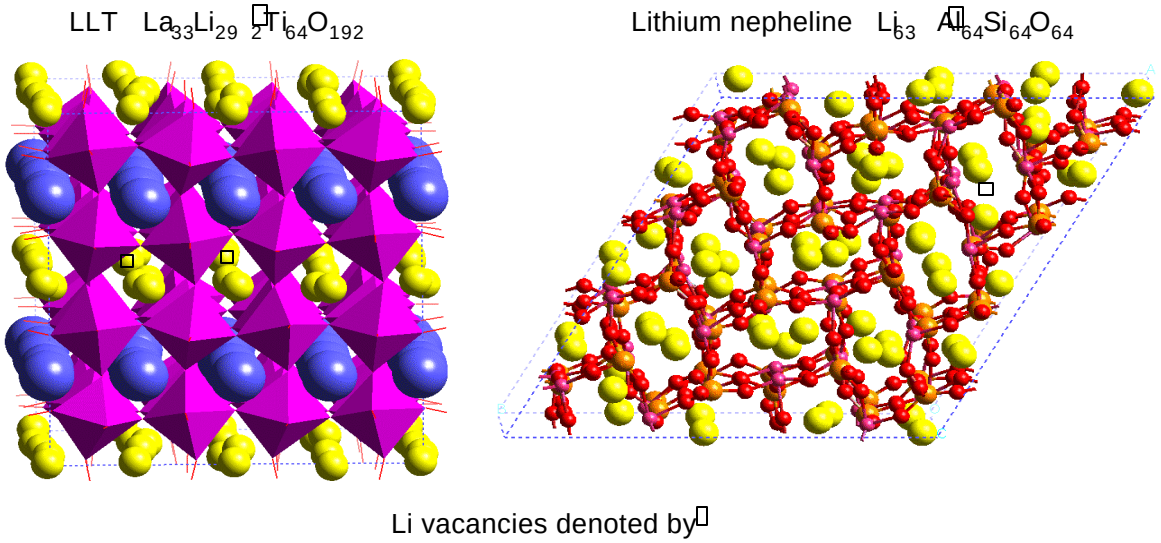

Figure 24. Simulations used in dynamic runs.

8. Integration.

With the cathode, anode and electrolyte in hand, integration of these components to form the ACB device were undertaken. Three arrangements were considered (a) standard, (b) inverted, and (c) side by side (Figure 1). Initial attempts focused on the standard arrangement. The film was analyzed by XRD (Figure 25) and each of the individual components are readily identified. This will allow us to study the battery's *in-situ* processes. Unfortunately, initial testing of this battery yielded only electrical shorts. To simplify the initial battery construction, the sol-gel SnO_2 anode was replaced with a sputter deposited Sn°.

The relatively high temperatures required to form the desired perovskite phase in the LLT-class of candidate electrolyte materials raised concern with respect to stack integration.

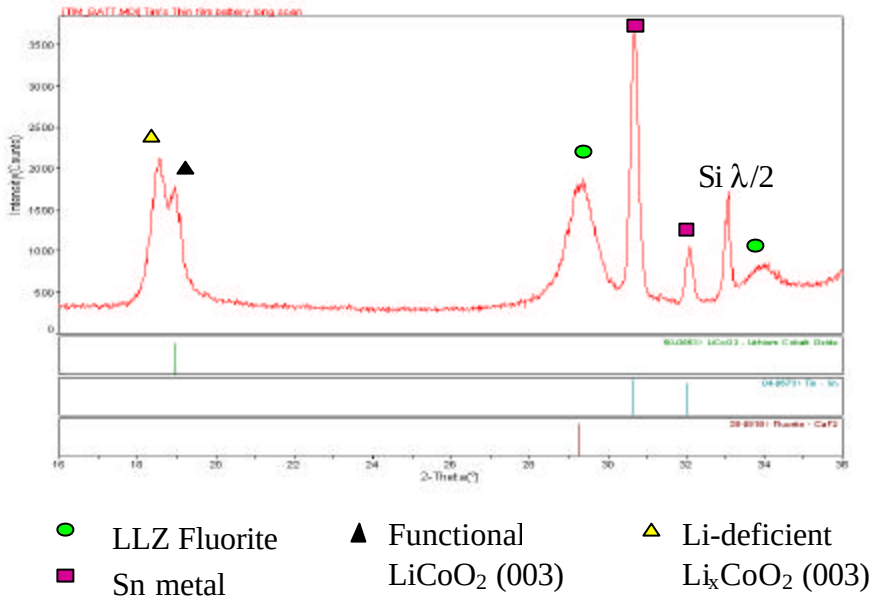

Figure 25. XRD pattern of full ACB.

The high crystallization temperatures of the LLT precursor layer on the Si/Pt/$LiCoO_2$ stack could cause layer inter-diffusion and loss of layer integrity. It was found that the different LLT materials could be converted to the perovskite phase by rapid thermal processing (RTP). The baseline RTP schedule was to heat a sample in flowing O_2 from room temperature to 900 ℃ in 3 seconds, hold for 65 seconds, and rapidly furnace cool. Using this schedule, LLT, LLZ, LLTa, and LLNb precursor films on the Si/Pt/$LiCoO_2$ stack were crystallized and then characterized by SEM. As a baseline for determining the effects of the RTP crystallization process on stack integrity, Figure 26 shows a SEM photomicrograph of a Si/Pt/$LiCoO_2$/LLNb stack (fracture cross-section) prior to the RTP operation.

The figure shows the distinct layers of the different ACB components. The layers appear dense and continuous, with some porosity being present at the $LiCoO_2$/LLNb interface. The $LiCoO_2$ cathode layer is composed of columnar grains indicating that nucleation occurred at

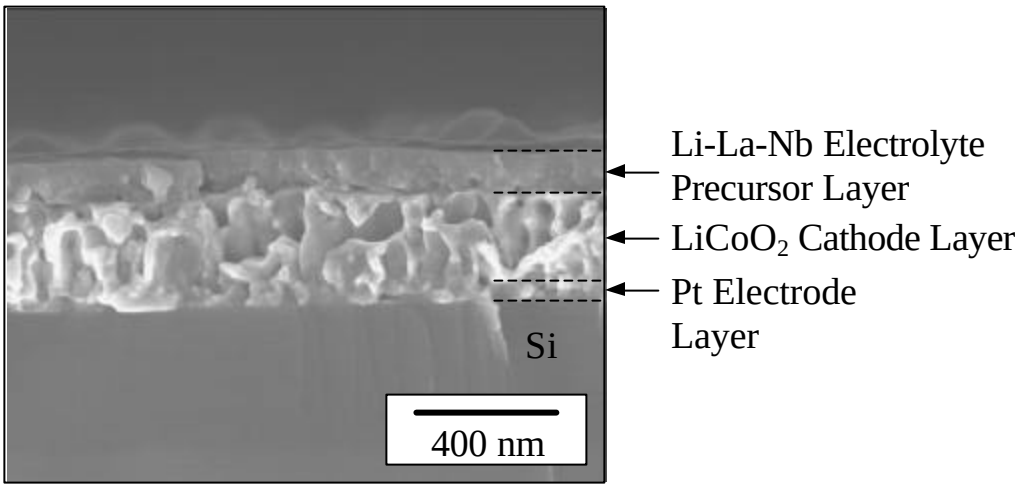

Figure 26. SEM photomicrograph of a fracture cross-section of a Si/Pt/$LiCoO_2$/LLNb stack prior to crystallization.

the Pt/$LiCoO_2$ interface when the sol gel-derived layer was crystallized. EDS was attempted to determine the degree of inter-diffusion between layers, but proved inconclusive due to the large sampling volume relative to the thickness of the layers and layer roughness.

Shown in Figures 26 - 30 are SEM photomicrographs of fracture cross-sections of the LLNb, LLT, LLZ, and LLTa stacks after RTP crystallization, respectively. A comparison of the LLNb film before (Figure 26) and after (Figure 27) the 900 °C crystallization step show that the film stack remains largely unchanged. The different layers remain distinct and continuous, the porosity at the $LiCoO_2$/LLNb interface remains, and there is good adherence between layers. It does appear that significant grain growth occurred in the $LiCoO_2$ layer – the grains are know longer columnar and have become "blocky". The LLT film (Figure 28) looks very similar to the LLNb film shown in Figure 27 with respect to residual porosity at the $LiCoO_2$/electrolyte interface.

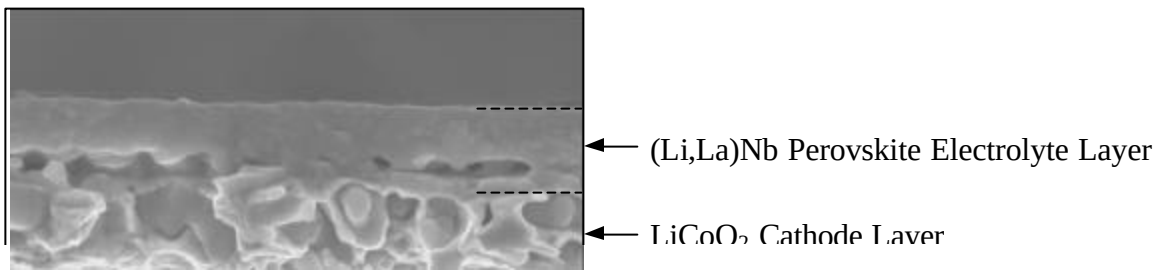

Figure 27. SEM photomicrograph of a fracture cross-section of a Si/Pt/$LiCoO_2$/LLNb stack after RTP at 900 °C.

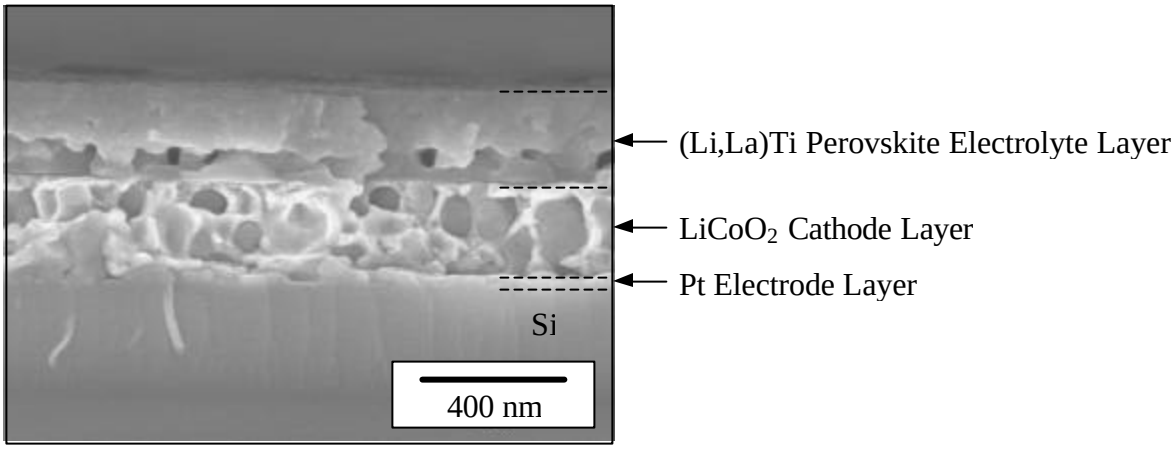

Figure 28.SEM photomicrograph of a fracture cross-section of a Si/Pt/$LiCoO_2$/LLT stack after RTP at 900 °C.

In contrast the LLZr (Figure 29) and the LLTa (Figure 30) have little or no porosity at this interface. The LLZr film appears to have a much finer grain structure than the other electrolyte materials. This is consistent with the Zr-based perovskite phase being difficult to crystallize in phase pure form.

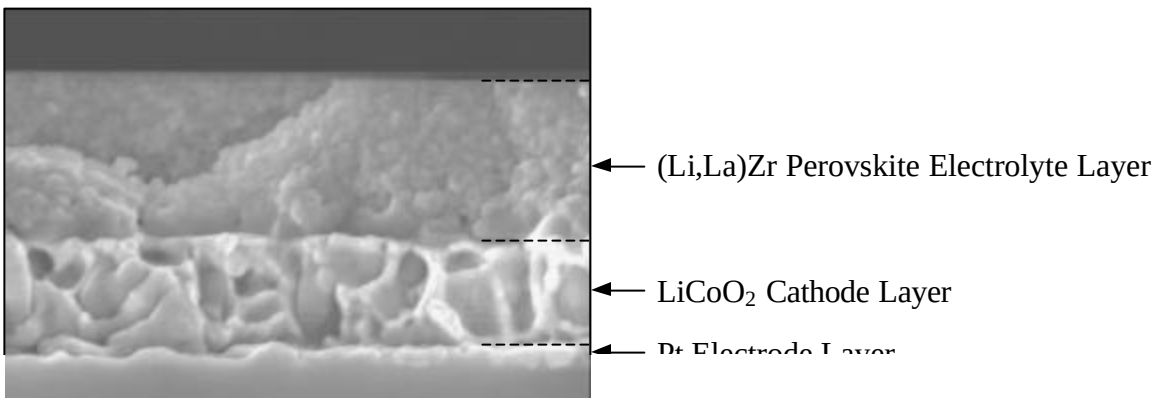

Figure 29. SEM photomicrograph of a fracture cross-section of a Si/Pt/$LiCoO_2$/LLZ stack

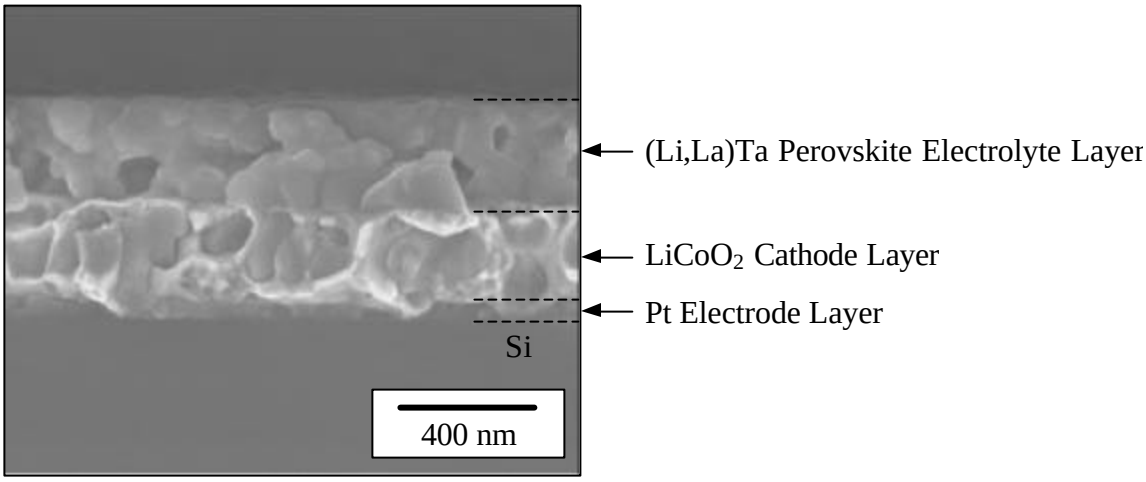

Figure 30. SEM photomicrograph of a fracture cross-section of a Si/Pt/$LiCoO_2$/LLTa stack after RTP at 900 °C.

From these data, it is readily apparent that uniform continuous films are generated for the electrolyte on the cathode. Improvements on the cathode are necessary to remove some of the particulate looking materials. From the above studies, LLT was chosen as the desired electrolyte for investigation due to the preferential perovskite formation and quality of the final film. Unfortunately, all testing of both standard ACB, inverted and side-by-side arrangements using the LLT electrolyte of the ACB proved to be shorted.

9. Summary of project

In our efforts to create an All Ceramic Thin Film Battery (ACB), we performed both fundamental and applied research related to all elements of the system, including the anode material, cathode material, the electrolyte material, as well as the substrate on which the structure is fabricated. Much of the initial work focused on the individual layers, and we were able to successfully develop each of these. After successful completion of these material development efforts, we then focused on the issues associated with integration of these structures into a finished device.

The initial aspect of this work focused on developing the optimal substrate necessary to orient the $LiCoO_2$ for maximum power. Since this oxide is a layered structure and since charge compensation occurs through the edge plane, it is necessary to orient the oxide layer perpendicular to the surface. While several different materials were shown to be acceptable in serving this role, empirical and molecular modeling calculations clearly demonstrated that either a Au° or Pt metallic substrate would be optimal for formation of oriented $LiCoO_2$. Based on these calculations we assumed that preparation of oriented thin films could be readily achieved, however this was not the case. In fact, a significant amount of effort exploring the phase space was necessary to achieve the objective.

These studies included evaluation of many experimental parameters for preparation of the orientated materials which included preparation of new compounds, development of novel solution preparation routes, as well as evaluation of the myriad processing variables themselves, including concentration, processing time and temperature. As a part of this work we developed several new and novel families of compounds. In addition, the processing parameters necessary to produce robust, high quality films were evaluated, and one of the critical processing

parameters identified was humidity of the environment during film preparation. The optimal formulation developed as a result of this work consists of a commercially available $Co(O_2CCH_3)_2$ (or $Co(OAc)_2$) and the novel $[Li(ONep)]_8$ in a pyridine/ toluene mixture which proved to be very stable. We also showed that the $LiCo(OAr)_3$ family of compounds would also produce a useable cathode material. The oriented films attained were textured having their layers 30° off normal to the plane of the substrate. That is, in an orientation necessary to allow charge compensation during operation. Furthermore, these films were found to be able to reversibly oxidized and reduced, i.e. charged/discharged.

In the case of the candidate negative electrode material, tin oxide, the situation was similar to that of the cobalt oxide, at least insofar as the availability of commercially available precursors, or the lack thereof. To meet this need, we developed a series of novel $Sn(OR)_2$ compounds. From this library of new compounds, we determined that high quality electrochemically active films could be prepared using the novel $[Sn(ONep)_2]_8$ in acetic acid. From investigations into the product of this reaction was determined to be $Sn_6(O)_4(ONep)_4$, a hydrolysis product due to uncontrolled esterification. Exploitation of this complex to generate more dense films (i.e., fewer layers) are underway.

Although none of the films was easily prepared, the electrolyte proved to be the most difficult of all. Initial attempts focused on developing a series of phase pure $LiLn(PO_3)_4$ materials. This was successfully realized, but due to the limited solubility and the successive dissolution of the cathode material upon deposition, which prevented formation of thick, defect-free films. In addition, the materials were very hygroscopic, which makes handling problematic. For these reasons we eliminated this material from further consideration. Literature reports indicated that $(Li,La)TiO_3$ (LLT) would be a very good alternative since it had high Li-ion

conductivity and was a perovskite material. High quality films of the phase pure LLT were finally prepared by using a mixture of normal and rapid thermal processing which was determined after a number of processing experimental arrays were investigated. However, these films were not defect-free over large areas, so the electrodes were invariably shorted (more will be said about this later).

Thin films of the ORMOLYTES were also successfully generated as a potential electrolyte layer. Numerous problems associated with crystallization of the material versus film formation were overcome. Ultimately a continuous thin film of the silica polymer were generated using a novel process however, these were not ionically conductive.

Finally, with the individual layers, integration of these components was undertaken. Examination by SEM analysis revealed that discrete continuous layers were formed. However, of the hundreds of devices prepared, all were electrically shorted. The reason for the shorting was never definitively identified, and our current thinking on this issue is that there is some ad-atom mixing during processing, or the electrolyte layer is not defect free over the large areas of the battery structures.

10. Conclusion.

During this project's tenure we have overcome numerous materials problems and we were able to generate the individual components of the ACB. Novel solution routes that involved newly synthesized and commercially available precursors were developed and used to generate the positive electrode material ($LiCoO_2$), the negative electrode material (SnO_x) (both of which were the original proposed material), and the electrolyte. The anode generated from an HOAc-modified $[Sn(ONep)_2]_8$ solution showed conversion of the cassiterite to Sn° after one cycle life.

This is consistent with literature reports and is typically compensated by additional cathode material. A rechargeable cathode, $LiCoO_2$ was synthesized from sol-gel methods using $[Li(ONep)]_8$ and $Co(OAc)_2$. Single-source precursors were also shown to be an effective means for preparing complex oxide materials such as $LiCoO_2$. A route to the perovskite phase of the electrolyte LLT was discovered using a solution of the novel compounds $[Li(ONep)]_8$, $[Ti(\mu\text{-}ONep)(ONep)_3]_2$, and $La(DIP)_3(py)_2$. The individual components were successfully integrated with little mixing based on SEM. Initial electrical testing of the hundreds of ACB devices prepared indicated that all were electrically shorted.

Due to the behavior of the individual components, it is expect that the construction of the ACB may have been achieved, but on a very small 2-D scale over which the electrolyte film is defect free, but which cannot be characterized with our current equipment due to the dimensional constraints. Part of our basis for this belief is based on a comparison of the films generated under this program with those developed under our PZT activity. In this case quality of the films generated here greatly exceeds what has been found for these other systems. However, in the case of the PZT activity where devices have been successfully prepared without shorting, very small top electrodes are utilized. By way of contrast, the top electrodes used in the ACB are 100's of times larger than those devices. It is believed that the observed electrical shorting, which is more an issue of the quality of the films, coupled with the lack of available instrumentation to measure very small currents as well as to allow electrical contact positioning is the issue that next needs to be addressed. Further work in developing alternative electrolytes and acquisition of the requisite equipment are necessary to prove the utility of the ACB.

11. References

(1) Jacoby, M. *C&E News* **August 3,1998**, *76*, 37.

(2) Doughty, D. H. *SAMPE Journal* **1996**, *32*, 75.

(3) Ohzuku, T. *Lithium Batteries. New Materials, Developments and Perspectives*; Elsevier Science B. V.: Dordrecht, 1994.

(4) Salomon, M.; Scrosati, B. *Gazzetta Chimica Italiana* **1996**, *126*, 415.

(5) Takehara, Z. *J. Power Sources* **1997**, *68*, 82.

(6) Hampden-Smith, M. J.; Wark, T. A.; Rheingold, A.; Huffman, J. C. *Can. J. Chem.* **1991**, *69*, 121.

(7) Reuter, H.; Kremser, M. *Z. Anorg. Allg. Chem.* **1991**, *598/599*, 259.

(8) Chandler, C. D.; Caruso, J.; Hampden-Smith, M. J.; Rheingold, A. L. *Polyhedron* **1995**, *14*, 2491.

(9) Smith, G. D.; Visciglio, V. M.; Fanwich, P. E.; Rothwell, I. P. *Organometallics* **1992**, *11*, 1064.

(10) Fjeldberg, T.; Hitchcock, P. B.; Lappert, M. F.; Smith, S. J.; Thorne, A. J. *Chem. Commun.* **1985**, 939.

(11) Veith, M.; Hobein, P.; Rosler, R. *Z. Naturforsch., Teil B* **1989**, *44*, 1067.

(12) Suh, S.; Hoffman, D. M.; Atagi, L. M.; Smith, D. C.; Liu, J.-R.; Chu, W.-K. *Chem. Mater.* **1997**, *9*, 730.

(13) Suh, S.; Hoffman, D. M. *Inorg. Chem.* **1996**, *35*, 6164.

(14) Gulliver, E. A.; Garvey, J. W.; Wark, T. A.; Hampden-Smith, M. J.; Datye, A. *J. Am. Cer. Soc.* **1991**, *74*, 1091.

(15) Hampden-Smith, M. J.; Wark, T. A.; Brinker, C. J. *Coord. Chem. Rev.* **1992**, *112*, 81.

(16) Matsumoto, T.; Murakami, Y.; Yahikozawa, K.; Takasu, Y. *Kagaku Kogaku Ronbunshu* **1995**, *21*, 1047.

(17) Howie, R. A.; Moser, W. *Nature* **1968**, *219*, 373.

(18) Harrison, P. G.; Haylett, B. J.; King, T. J. *Chem. Commmun.* **1978**, 112.

(19) Sasaki, Y.; Miyazawa, N. *Kin. Daigaku Rik. Kenk. Hokoku* **1992**, *28*, 237.

(20) Yang, C. B.; Tung, J. Y.; Chen, J. H.; Liao, F. L.; Wang, S. L.; Wang, S. S.; Hwang, L. P. *J. Chem. Cryst.* **1998**, *28*, 481.

(21) Tsai, C. C.; Chen, Y. j.; Chen, J. H.; Hwang, L. P. *Polyhedron* **1992**, *11*, 1647.

(22) Sita, L. R.; Xi, R.; Yap, G. P. A.; Liable-Sands, L. M.; Rheingold, A. L. *J. Am. Chem. Soc.* **1997**, *119*, 756.

(23) Reuter, H.; Kremser, M. *Z. Anorg. Allg. Chem.* **1992**, *615*, 137.

(24) Harris, D. H.; Lappert, M. F. *Chem. Commun.* **1974**, 895.

(25) Bradley, D. C.; Mehrotra, R. C.; Gaur, D. P. *Metal Alkoxides*; Academic Press: New York, 1978.

(26) Olmstead, M. M.; Power, P. P. *Inorg. Chem.* **1984**, *23*, 413.

(27) Boyle, T. J.; Alam, T. M.; Rodriguez, M. A.; Zechmann, C. A. *Inorg. Chem.* **2002**, *41*, 25742.

(28) Boyle, T. J.; Segall, J. M.; Alam, T. M.; Rodriguez, M. A.; Santana, J. M. *J. Am. Chem. Soc.* **2002**, *124*, 6904.

(29) Boyle, T. J.; Al-Shareef, H. N.; Buchheit, C. D.; Cygan, R. T.; Dimos, D.; Rodriguez, M. A.; Scott, B.; Ziller, J. W. *Integrated Ferroelectrics* **1997**, *18*, 213.

(30) Boyle, T. J.; Al-Shareef, H. N. *J. Mater. Sci.* **1997**, *32*, 2263.

(31) Armstrong, R. A.; Bruce, P. G. *Nature* **1996**, *381*, 499.

(32) Thackeray, M. M. *J. Electrochem. Soc.* **1995**, *142*, 2558.

(33) Thackeray, M. M. *Prog. Solid State Chem.* **1997**, *25*, 1.

(34) Banner, J. A.; Winchester, C. S. *J. Power Sources* **1997**, *65*, 271.

(35) Florjanczyk, Z.; Zygadlomonikowska, W.; Bzducha, W.; Borkowska, R. *Polimery* **1996**, *41*, 391.

(36) Koksbang, R.; Barker, J.; Shi, H.; Saidi, M. Y. *Solid State Ionics* **1996**, *84*, 1.

(37) Park, Y. J.; Kim, J. G.; Kim, M. K.; Kim, H. G.; Chung, H. T.; Park, Y. *J. Power Sources* **2000**, *87*, 69.

(38) Kang, K.; Dai, S. H.; Wan, Y. H. *J. Inorg. Materials* **2001**, *16*, 586.

(39) Zhang, W. M.; Yang, Y. H.; Sun, S. X.; Liu, Z. P.; Song, X. Y. *Chinese, J. Inorg. Chem.* **2000**, *16*, 873.

(40) Ammundsen, B.; Paulsen, J. *Adv. Materials* **2001**, *13*, 943.

(41) Scrosati, B. *Electrochimica Acta* **2000**, *45*, 2461.

(42) Chen, C. H.; Buysman, A. A. J.; Kelder, E. M.; Schoonman, J. *Solid State Ionics* **1995**, *80*, 1.

(43) Boyle, T. J.; Ingersoll, D.; Alam, T. M.; Tafoya, C. J.; Rodriguez, M. A.; Vanheusden, K.; Doughty, D. H. *Chem. Mater.* **1998**, *10*, 2270.

(44) Boyle, T. J.; Voigt, J. A.; Section 52-2 (Electrochemical, Radiational, and Thermal Energy Technology): US 5630994, 1997; Vol. Main IPC C01G045-12, p 6.

(45) Boyle, T. J.; Ingersoll, D.; Rodriguez, M. A.; Tafoya, C. J.; Doughty, D. H. *J. Electrochem. Soc.* **1999**, *146*, 1683.

(46) Tullo, A. H. *Chemical & Engineering News* **2002**, 25.

(47) Boyle, T. J.; Rodriguez, M. A.; Ingersoll, D.; Pedrotty, D. M.; De'Angeli, S. M.; Vick, S. C.; Bunge, S. D.; Fan, H.-Y. *Chemistry of Materials* **2002**, (submitted).

(48) Boyle, T. J.; Alam, T. M.; Peters, K. P.; Rodriguez, M. A. *Inorg. Chem.* **2002**, *40*, 6281.

(49) Nairn, K. M.; Forsyth, M.; Greville, M.; MacFarlane, D. R.; Smith, M. E. *Solid State Ionics* **1996**, *86-8*, 1397.

(50) Takai, S.; Moriyama, M.; Esaka, T. *Materials Science Forum*, *269*, 93.

(51) Inagumay, Y.; Chen, L. Q.; Itoh, M.; Nakamura, T.; Uchida, T.; Ikuta, H.; Wakihara, M. *Solid State Communications* **1993**, *86*, 689.

(52) Boyle, T. J.; Alam, T. M.; Mechenbeir, E. R.; Scott, B.; Ziller, J. W. *Inorg. Chem.* **1997**, *36*, 3293.

(53) Butcher, R. J.; Clark, D. L.; Grumbine, S. K.; Vincent-Hollis, R. L.; Scott, B. L.; Watkin, J. G. *Inorg. Chem.* **1995**, *34*, 5468.

(54) Boyle, T. J.; Gallegos III, J. J.; Pedrotty, D. M.; Mechenbier, E. R.; Scott, B. L. *J. Coord. Chem.* **1999**, *47*, 155.

(55) Boyle, T. J.; Alam, T. M.; Dimos, D.; Moore, G. J.; Buchheit, C. D.; Al-Shareef, H. N.; Mechenbier, E. R.; Bear, B. R. *Chem. Mater.* **1997**, *9*, 3187.

(56) Cygan, R. T.; Westrich, H. R.; Doughty, D. H. In *Materials for Electrochemical Storage and Conversion—Batteries, Capacitors and Fuel Cells*; Doughty, D. H. e. a., Ed.; Materials Research Society: Pittsburgh, 1995, p 113.

(57) Cygan, R. T.; Westrich, H. R.; Doughty, D. H. In *Materials for Electrochemical Storage and Conversion II—Batteries, Capacitors and Fuel Cells*; Ginley, D. S. e. a., Ed.; Materials Research Society: Pittsburgh, 1998.

(58) Gummow, R. J.; Liles, D. C.; Thackeray, M. M.; David, W. I. F. *Mater. Res. Bull.* **1993**, *28*, 1174.

(59) Bates, J. B.; Dudney, N. J.; Neudecker, B. J.; Hart, F. X.; Jun, H. P.; Hackney, S. A. *J. Electro. Soc.* **2000**, *147*, 59.

(60) Rappé, A. K.; Casewit, C. J.; Colwell, K. S.; Goddard, W. A.; Skiff, W. M. *J. Am. Chem. Soc.* **1992**, *114*, 10024.

(61) Je, J. H.; Noh, D. Y.; Kim, H. K.; Liang, K. S. *J. Mater. Res.* **1997**, *12*, 9.

(62) Bohnke, O.; Bohnke, C.; Fourquet, J. L. *Sol. St. Ionics* **1996**, *91*, 21.

(63) Sato, M.; Abo, J.; Jin, T.; Ohta, M. *J. Alloys Compd.* **1993**, *192*, 81.

(64) Foreman, N.; Peacor, D. R. *Z. Krist.* **1970**, *132*, 45.

(65) Wyckoff, R. G. W. *Crystal Structures*; John Wiley and Sons: New York., 1963.

(66) Isasi, J.; Veiga, M. L.; Fernandez, F.; Pico, C. *J. Mater. Sci.* **1996**, *31*, 4689.

(67) Hyooma, H.; Hayashi, K. *Mater. Res. Bull.* **1988**, *23*, 1399.

(68) Moseley, P. T.; Crocker, A. J.; Crocker, J.; Moseley, P. *Sensor Materials*; Institute of Physics Publications: New York, 1997.

(69) Inaguma, Y.; Itoh, M. *Sol. St. Ionics* **1996**, *86-88*, 257.

(70) Inaguma, Y.; Chen, L.; Itoh, M.; Nakamura, T. *Sol. St. Ionics* **1994**, *70/71*, 196.

(71) Fu, J. *Sol. St. Ionics* **1997**, *96*, 195.

(72) Katsumata, T.; Inaguma, Y.; Itoh, M.; Kawamura, K. *J. Ceram. Soc. Jpn* **1999**, *107*, 615.

(73) Teter, D. M. *Phys. Rev. Lett.* **2002 (submitted)**.

(74) Dauber-Osguthorpe, P.; Roberts, V. A.; Osguthorpe, D. J.; Wolff, J.; Genest, M.; Hagler, A. T. *Proteins: Structure, Function, and Genetics* **1988**, *4*, 31.

12. Distribution List

Personnel	Group	Mail stop	Copies
Timothy J. Boyle	1846	1349	5
David Ingersoll	2521	0613	5
Randall T. Cygan	6118	0750	2
Mark A. Rodriguez	1822	1411	2
Kamyar Rahimian	1846	0888	2
James A. Voigt	1846	1411	2
William F. Hammetter	1846	1349	2
Daniel H. Doughty	2521	0613	2
Barrett G. Potter Jr.	1846	1411	2
Duane B. Dimos	1801	0885	1
Michael Cieslak	1800	0887	1
Central Technical Files	8945-1	9018	1
Technical Library	9616	0899	2
Review and Approval Desk	9612	0612	1